

# CLUSTER and IMAGE: New Ways to Study the Earth's Plasmasphere

Johan De Keyser · Donald L. Carpenter ·  
Fabien Darrouzet · Dennis L. Gallagher · Jiannan Tu

Received: 5 June 2008 / Accepted: 5 November 2008 / Published online: 8 January 2009  
© Springer Science+Business Media B.V. 2009

**Abstract** Ground-based instruments and a number of space missions have contributed to our knowledge of the plasmasphere since its discovery half a century ago, but it is fair to say that many questions have remained unanswered. Recently, NASA's IMAGE and ESA's CLUSTER probes have introduced new observational concepts, thereby providing a non-local view of the plasmasphere. IMAGE carried an extreme ultraviolet imager producing global pictures of the plasmasphere. Its instrumentation also included a radio sounder for remotely sensing the spacecraft environment. The CLUSTER mission provides observations at four nearby points as the four-spacecraft configuration crosses the outer plasmasphere on every perigee pass, thereby giving an idea of field and plasma gradients and of electric current density. This paper starts with a historical overview of classical single-spacecraft data interpretation, discusses the non-local nature of the IMAGE and CLUSTER measurements, and emphasizes the importance of the new data interpretation tools that have been developed to extract non-local information from these observations. The paper reviews these innovative techniques and highlights some of them to give an idea of the flavor of these methods.

---

J. De Keyser (✉) · F. Darrouzet  
Belgian Institute for Space Aeronomy, Ringlaan 3, 1180 Brussels, Belgium  
e-mail: [Johan.DeKeyser@aeronomie.be](mailto:Johan.DeKeyser@aeronomie.be)

F. Darrouzet  
e-mail: [Fabien.Darrouzet@aeronomie.be](mailto:Fabien.Darrouzet@aeronomie.be)

D.L. Carpenter  
Space Telecommunications and Radioscience Laboratory, Stanford University, Stanford, CA, USA  
e-mail: [dlc@nova.stanford.edu](mailto:dlc@nova.stanford.edu)

D.L. Gallagher  
NASA Marshall Space Flight Center, National Space Science & Technology Center, Huntsville, AL,  
USA  
e-mail: [dennis.l.gallagher@nasa.gov](mailto:dennis.l.gallagher@nasa.gov)

J. Tu  
Center for Atmospheric Research, University of Massachusetts Lowell, Lowell, MA, USA  
e-mail: [Jiannan\\_Tu@uml.edu](mailto:Jiannan_Tu@uml.edu)

In doing so, it is shown how the non-local perspective opens new avenues for plasmaspheric research.

**Keywords** Plasmasphere · CLUSTER · IMAGE · Measurement techniques

## 1 Introduction

Sixty years ago, Owen Storey inferred the existence of a dispersive medium in near-Earth space in order to explain the propagation of whistler radio waves along the geomagnetic field lines. This medium is now known as the “plasmasphere”. In 1959 Gringauz’ plasma instrument on LUNIK 2 provided an in situ confirmation of its existence. The plasmasphere has been studied ever since. NASA’s Imager for Magnetopause-to-Aurora Global Exploration, IMAGE (Burch 2000), and ESA’s CLUSTER probes (Escoubet et al. 1997) have ushered in a new era of plasmaspheric research through innovative observation strategies. The goal of this paper is to highlight these observation techniques and the new data interpretation methods they require, in order to show how they can advance our scientific understanding of the plasmasphere.

The plasmasphere does not easily reveal its secrets. One of the major difficulties has been the low temperature of the plasmaspheric plasma (a few eV at most). Spacecraft potential control and appropriately biased detectors are required to properly sample this cold population. Separating the photo-electrons from the plasmaspheric electrons is another problem. The inner magnetosphere contains cold plasmaspheric plasma, warm ring current particles, and energetic radiation belt particles, so that a comprehensive study necessitates an instrument suite that covers a wide energy range. The densities of these populations vary over several orders of magnitude and the plasma composition is variable, with important contributions from heavier ions of ionospheric origin.

The plasmasphere is subject to the solar wind induced magnetospheric electric field at high altitude, as well as to the forcing by the ionosphere at low altitude. As a consequence, the plasmasphere undergoes a cyclic evolution. Upon arrival of a solar wind disturbance at Earth, the flank-to-flank electric potential difference across the magnetosphere increases and the roughly dawn-to-dusk electric field becomes stronger, so that the outer regions of the plasmasphere are eroded away. The plasmasphere develops a sharp outer density gradient, known as the plasmopause. If the disturbance is strong enough, the eroded material can form a plume in the afternoon local time sector, sometimes reaching out to the dayside magnetopause. The nightside edge of the plume footpoint appears to coincide with the intense electric fields associated with ionospheric subauroral ion drifts or subauroral polarization streams. As the magnetospheric electric field recovers, the plasmasphere is refilled from the ionosphere on a time scale of hours or even days, thus becoming denser and larger in average radius, and exhibiting a locally less well defined outer boundary. As quieting proceeds, an existing plume may begin to rotate with the Earth, move outward, and eventually disappear.

The plasmasphere is a dynamic system with memory: Its spatial structure bears the imprint of past changes in the magnetospheric electric field, while refilling tends to smooth away all structure. Solar wind perturbations (with varying duration, intensity, and recurrence frequency), as well as variations in the ionosphere as a refilling plasma source, produce a zoo of spatio-temporal structures. Single-spacecraft measurements cannot separate variations in different spatial directions or distinguish spatial from temporal effects. It is especially in this domain that the IMAGE and CLUSTER probes have offered what previous spacecraft could not: a non-local perspective.

The purpose of this paper is to illustrate in what ways IMAGE and CLUSTER can open up new directions of plasmaspheric research. To set the scene, Sect. 2 briefly recalls what we knew about the plasmasphere from ground-based radio sounding and from classical single-spacecraft measurements. Section 3 explains the rationale of the non-local measurement techniques introduced by IMAGE and CLUSTER. In Sect. 4 we discuss new analysis tools for extracting non-local information from the data, without trying to be exhaustive. We focus on a few of those tools in more detail to give an idea of the typical difficulties that are encountered and how they can be solved, and of the potential pay-off of such techniques. Scientific results obtained with these techniques are reviewed in the accompanying papers (Darrouzet et al. 2008; Matsui et al. 2008; Masson et al. 2008; Pierrard et al. 2008; Reinisch et al. 2008, this issue). Section 5 concludes the paper and offers an outlook.

## 2 History of Plasmasphere Data Interpretation

In this section we illustrate the fundamental modes of data interpretation that have been used prior to IMAGE and CLUSTER, so that the significance of the new analysis methods used in conjunction with those missions can be more fully appreciated. We discuss plasmasphere data interpretation by highlighting a few historical milestones; a more complete account of the history of plasmaspheric research before the IMAGE and CLUSTER missions can be found in the monograph by Lemaire and Gringauz (1998). Other historical reviews are the papers by Gringauz and Bezrukikh (1977), Ganguli et al. (2000), Carpenter (2004), and Kotova (2007).

### 2.1 Data Interpretation at the Beginning of the Space Age

The discovery of the plasmasphere and its outer boundary, the plasmopause, is itself a nice illustration of the role of different experimental techniques and the associated data interpretation.

The first hint at the existence of the plasmasphere came from remote sensing. In the late 1940s, Storey used observations of whistlers, dispersed radio signals from lightning, to determine that the essentially geomagnetic-field aligned paths of whistlers extended several Earth radii ( $R_E$ ) into space at the equator (Storey 1953). Theoretical considerations allowed him to conclude that the plasma density at those peak altitudes was  $\sim 400 \text{ cm}^{-3}$ , orders of magnitude higher than conventional wisdom would predict, based on the assumption of an oxygen-dominated upper atmosphere. Some years later, Carpenter used data from a spatial network of whistler receivers established in 1957–1958 to identify a knee-like drop-off in the range  $2 < L < 5$  ( $L$  being McIlwain's parameter, approximately the radial distance of the equatorial point on a field line expressed in  $R_E$ , McIlwain 1961) in the equatorial profile of electron density (Carpenter 1963). In 1959, Gringauz and his colleagues of the Radio Technical Institute in Moscow placed ion traps on LUNIK 1 and 2, destined for impact on the moon. As the spacecraft were underway, their in situ measurements revealed both a region of plasma density comparable to the one identified by Storey as well as an unexpected falloff in that density at an altitude of  $\sim 10000 \text{ km}$  (Gringauz et al. 1960; Gringauz 1963), as shown in Fig. 1. The LUNIK measurements were met with some skepticism, and there apparently was some concern in the Soviet Academy of Sciences about the embarrassment that might attend the publication of an incorrect interpretation of the data (Lemaire and Gringauz 1998). The remote sensing and the in situ data seemed to contradict the theoretical predictions at that time. There remained an undercurrent of disbelief, which dissipated in 1963 when

**Fig. 1** Ion densities measured by LUNIK 2 (dots) and equatorial electron density profile from ground-based whistler measurements (solid curve) as a function of geocentric distance. The first line of numbers represents the invariant latitudes of the LUNIK 2 measurements, and the second line their latitudes. (From Carpenter 1965)

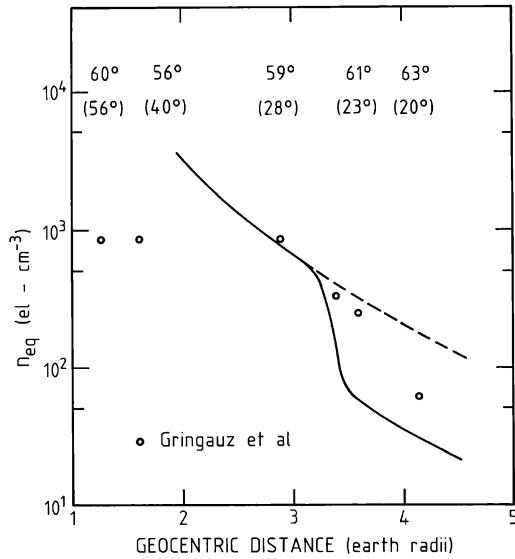
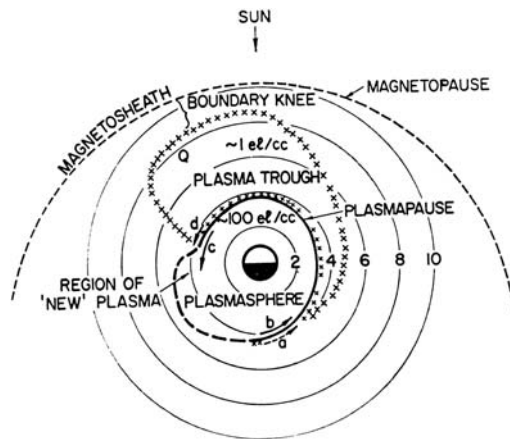


**Fig. 2** Average equatorial radius of the plasmasphere during multi-day periods of moderate disturbance following weak magnetic storms ( $K_p \approx 6$ ). The  $\times$ -symbols enclose regions most frequently probed by ground-observed whistlers that propagated outside the plasmasphere. Dashed lines indicate an evening sector region where the outer limits of the plasmasphere were not well defined in available whistler data. (From Carpenter 1966)



Gringauz and Carpenter met for the first time and when Fig. 1 was shown, illustrating their mutually consistent results (Carpenter 1965). As of today, the combined analysis of remote sensing and in situ data remains an important way of cross-checking results. In particular, the combination of IMAGE remote sensing and in situ CLUSTER measurements has proven to be very useful (e.g., Darrouzet et al. 2006a).

The whistler measurements were repeated in time, but also in space as more ground stations were deployed. Piecing together the abundant whistler data that became available from Antarctica in the early 1960s, Carpenter (1966) was able to estimate the average shape of what was now called the plasmasphere (Fig. 2). An evening bulge in radius was found. The density knee appeared to develop in the aftermath of magnetic disturbances and its equatorial radius was found to vary inversely with the intensity of the disturbance. Inward displacements of the knee on the night side were observed to correlate with the  $K_p$  index during the onsets of several weak magnetic storms, so that  $K_p$  became the dominant parameter in performing plasmaspheric studies.

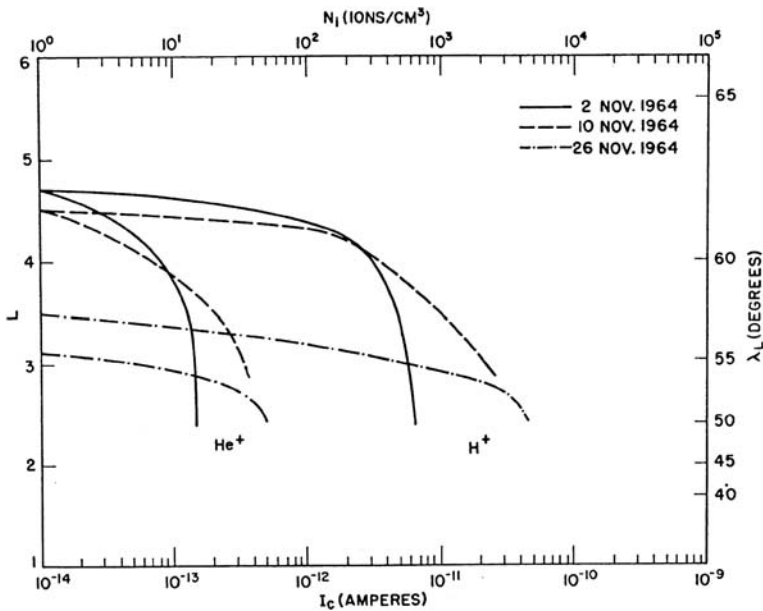


**Fig. 3** Profiles of  $\text{He}^+$  and  $\text{H}^+$  density versus altitude showing steep falloffs between  $L = 3$  and  $L = 5$ , measured by an ion mass spectrometer on board OGO 1. (From Taylor et al. 1965)

Those early days also showed that one had to be very careful with in situ data. The retarding potential electron analyzers on IMP 1 and IMP 3 had found no “knee” in the thermal plasma profile (Serbu and Maier 1967), while the effect was clearly seen by the retarding ion mass spectrometer on OGO 1 (see Fig. 3), (Taylor et al. 1965). A debate on the reality of the knee effect as identified from whistlers was held at the XV<sup>th</sup> URSI General Assembly in 1966. In the aftermath of the debate, a consensus developed that the retarding potential analyzers had suffered from the effects of an increase in spacecraft potential (Gurnett and Scarf 1967). This interference of the spacecraft potential with cold plasma spectrometer measurements is still a major challenge. Experimenters confront it by means of active spacecraft potential control and/or by biasing the plasma spectrometer; on CLUSTER this is done by means of the ASPOC ion current emitter and by the CIS/CODIF spectrometer’s RPA mode (Escoubet et al. 1997).

Many fundamental questions about plasmasphere dynamics have been addressed by means of extended time series of whistler measurements. A major question was whether the dayside upward fluxes from the ionosphere were sufficient to enable the plasmasphere to act as a night-time reservoir for the decaying ionospheric layers below. Some theorists suggested that a diffusive barrier between the  $\text{O}^+ - \text{H}^+$  charge exchange region of the ionosphere and the higher altitude level above which  $\text{H}^+$  becomes the dominant constituent would limit the upward  $\text{H}^+$  flux to a value less than that required for a replenishment of the night-time ionosphere (e.g., Hanson and Ortenburger 1961). Using electron density data from a library of Antarctic whistlers covering a long magnetic storm recovery period, Park (1970) showed both on a day-to-day basis and during a multi-hour period on a single day that the inferred upward fluxes could account for the drainage fluxes needed to replenish the ionosphere at night.

The interplay between solar-wind induced convection and plasma flow induced by the Earth's rotation was demonstrated at an early point by the evening bulge in the plasmasphere radius (Carpenter 1966). As suggested in Fig. 2, the bulge was not believed to be the result of radially outward drift of plasmas as local time increased in the late afternoon sector, but it was initially interpreted as representing plasma accumulated during the course of sunward convection. Once formed, the bulge was found to vary in terms of the local time at which its westward edge was first detected by a whistler ground station, appearing at earlier local times as magnetospheric disturbance levels increased (Carpenter 1970b). Later it became clear that the bulge as detected by a whistler station represented either a small remnant plume or that part of the westward edge of a plume nearest the main plasmasphere (Ho and Carpenter 1976; Carpenter et al. 1992, 1993, note that these papers did not use the term "plume" yet). The plasmasphere bulge was the impetus for the earliest theoretical efforts to explain the plasmopause phenomenon in terms of large-scale convection (e.g., Nishida 1966; Brice 1967). Dungey (1967) posed a problem about the plasmopause density profile that has persisted to the present day: He suggested that the unsteadiness in convection activity should lead to patchiness in the profile, a patchiness that would be inconsistent with the sharpness of the plasmopause. At the time, the whistler method was capable of identifying an order of magnitude density jump along the outermost detected whistler propagation path in the plasmasphere and the innermost one in the plasmatrough. However, it was not well capable of identifying fine structure near the plasmopause on a scale of  $0.1 R_E$  or less, or measuring its distribution as a function of equatorial radius and longitude (e.g., Carpenter 1970a). Detailed study of this structure therefore remained as a challenge to future experimenters.

## 2.2 More Refined Space Experiments

As noted, particle detectors that measure total plasma density in the plasmasphere and beyond can be subject to problems with instrument calibration and limitations, particularly for the colder or more tenuous plasma components. Nevertheless, such detectors have proven very useful in identifying important plasmasphere features. The increasing sophistication of the detectors has been accompanied by an increasing importance of the data interpretation techniques, for instance to ensure a proper calibration by relating the measured densities to those obtained from the radio detection of local wave resonances, which has proven to be highly accurate over a wide range of density levels.

In situ exploration in the 1960s and 1970s collected a large number of plasmaspheric ion number density profiles, such as those from the Russian satellites ELECTRON 2 and 4 by Bezrukikh (1970), thereby confirming the reality of the plasmopause density gradient. OGO 1 contributed the first profiles at high altitude of the proton and helium ion concentrations as depicted in Fig. 3 (Taylor et al. 1965), showing that the density gradient appears at the same place for both, with helium ions being less abundant (the density falloffs in Fig. 3 are larger than later studies of plasmatrough levels would support). The ISIS and OGO 2 and 4 polar orbiters gave the first insights into phenomena that were apparently associated with the projection of the plasmopause to ionospheric altitudes. The so-called lower hybrid resonance (LHR) noise band (Brice and Smith 1965) was found to serve as a marker of the plasmopause projection in ALOUETTE satellite measurements of whistler-mode wave activity. It was particularly well defined during periods of moderate to heavy magnetic disturbance and at times of substantial whistler activity. The spectrograms of Fig. 4 show two effects that occurred as ALOUETTE 1 moved poleward in the plasmopause region: (i) a falloff in whistlers propagating on paths through the outer plasmasphere from lightning sources in the conjugate region; (ii) a "breakup" in a noise band, involving a change in smoothness within  $\sim 1$  s and a drop in

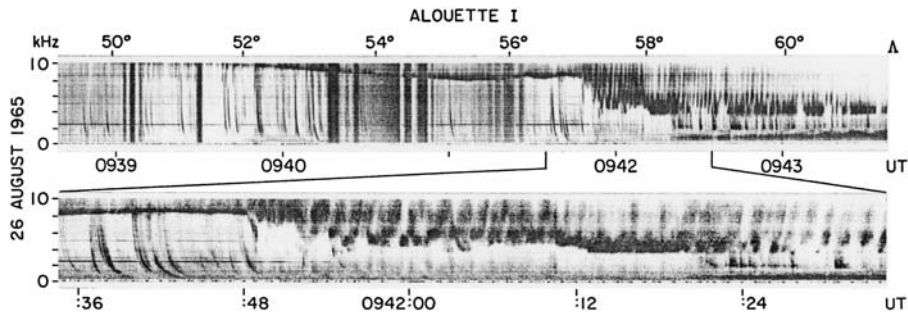


**Fig. 4** ALOUETTE 1 broadband VLF spectrograms (0–10 kHz versus time) showing abrupt changes in whistler and noise band activity near  $L = 3$  at  $\sim 04:40$  MLT. The abrupt changes were attributed to the projection of the plasmopause to 1000 km altitude. (Adapted from Carpenter et al. 1968)

lower cutoff frequency from  $\sim 8$  kHz to 4 kHz within 20 s (Carpenter et al. 1968). A proper knowledge of the behaviour of the waves was indispensable to interpret these changes in the local LHR frequency in terms of a spatial increase in the effective mass of the ions along the satellite orbit. These observations were also consistent with the discovery from OGO 2 of a light ion trough in the ionosphere just poleward of the plasmopause (Taylor et al. 1969), the plasmopause having been identified both by a falloff in whistlers from the conjugate region as well as a latitudinal dropoff in the strength of signals from powerful ground-based very low frequency (VLF) transmitters (Heyborne et al. 1969). Abrupt spatial transitions in whistler-mode wave activity were used as a basis for identifying a thermal linkage between the plasmasphere and ionosphere near the plasmopause (e.g., Carpenter 1971).

Among the more compelling observations of plasmasphere structure projected onto the ionosphere were OGO 4 measurements of a plume-like (using present-day terminology) feature that appeared in conjugate hemispheres just poleward of the main plasmasphere (Taylor et al. 1969). The feature was observed in  $H^+$  density on successive orbits, as illustrated in Fig. 5a, and was interpreted as the ionospheric projection of the plume at high altitude shown in Fig. 5b.

The first evaluation of plasmaspheric ion temperature was made with the LUNIK data (Gringauz et al. 1962), and later on with IMP 2 and OGO 5 (Serbu and Maier 1966, 1970). Those early measurements were neither reliable nor comprehensive enough to describe the thermal structure of the plasmasphere.

The harvest of plasmasphere observations from OGO 3 (Taylor et al. 1968), ELECTRON 2 and 4 (Bezrukikh 1970), and OGO 5 (Chappell et al. 1970), coupled with the ongoing whistler observations (Carpenter 1963, 1967), allowed scientists to use statistical data interpretation techniques successfully. These studies showed clearly that the plasmopause position can vary over a wide range of  $L$  values, from  $\sim 2$  to  $7 R_E$  (Fig. 6). The datasets from the Russian PROGNOZ satellites helped to infer the overall shape of the plasmasphere. They highlighted the asymmetrical shape of the plasmasphere, depending on the level of geomagnetic activity. Other studies confirmed that the plasmasphere was more extended on the day side than in the post-midnight sector (Bezrukikh and Gringauz 1976). Such studies were, of course, limited by the assumption that the observed structures were really spatial, rather than being due to changes in time: Only geomagnetic activity had been used to sort the data.

GEOS 1 and 2, launched in 1977 and 1978, carried three experiments to measure ion and electron densities: a mass spectrometer, a relaxation sounder, and a mutual impedance

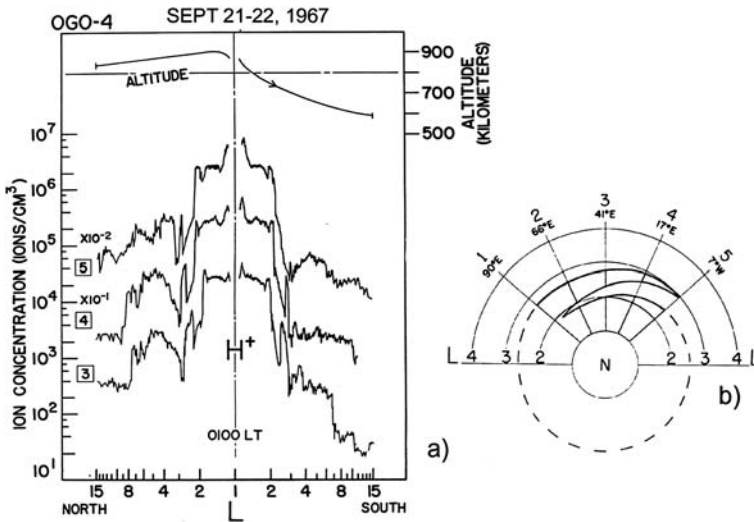


**Fig. 5** (a) A sequence of  $H^+$  density profiles acquired by an ion mass spectrometer on OGO 4, showing an inner trough that was detected in both hemispheres and was displaced outward with time. (b) Schematic representation of the plume-like structure derived from the series of five passes ending with those of part (a). The structure indicated is believed to have corotated relative to the essentially fixed local time of the satellite orbit. (From Taylor et al. 1971)

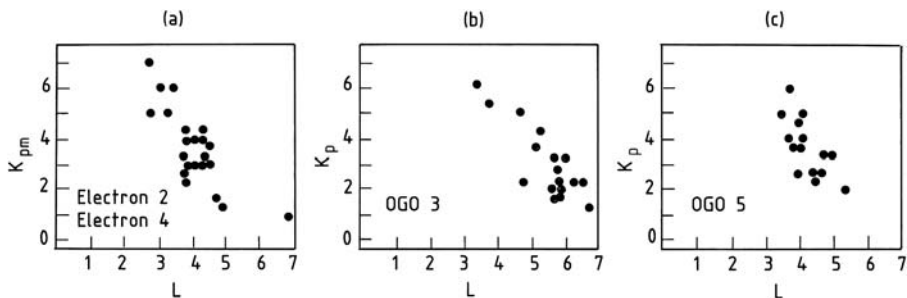


**Fig. 6**  $L$  position of the plasmapause as a function of the  $K_p$  average over the preceding 24 hours: (a) from ELECTRON 2 and ELECTRON 4, after Bezrukikh (1970); (b) from OGO 3, after Taylor et al. (1968); (c) from OGO 5, after Chappell et al. (1970)

experiment. Figure 7 shows results obtained with this last instrument onboard GEOS 1 on a pass beyond  $L = 4$  in the post-dusk sector in June 1978 (Décréau et al. 1982). There is a sharp change in density at what is marked as the plasmapause (PP in the figure), as well as an increase in temperature with  $L$ , as found with PROGNOZ 5 before. The mass spectrometer onboard GEOS 1 led to the first identification of  $D^+$ ,  $He^{++}$ , and  $O^{++}$  in the plasmasphere (Geiss et al. 1978). The diversity of these measurements reflects the sophistication of the instrumentation and offered a new challenge to data interpretation, in particular with respect to the origin and relative abundance of the heavy ion populations.

The plasma composition experiment on ISEE 1, launched in 1977, measured the  $H^+$  temperature. Statistical studies revealed that the mean temperature increases with  $L$ , both on the day and the night side (Fig. 8). On the day side, however, there is a negative temperature

**Fig. 7** Electron density and temperature profiles measured by GEOS 1 as a function of  $L$ , UT and MLT. The plasmapause is indicated by PP and  $P_1$  and  $P_2$  represent the  $L^{-4}$  profiles. (From Décréau et al. 1982)

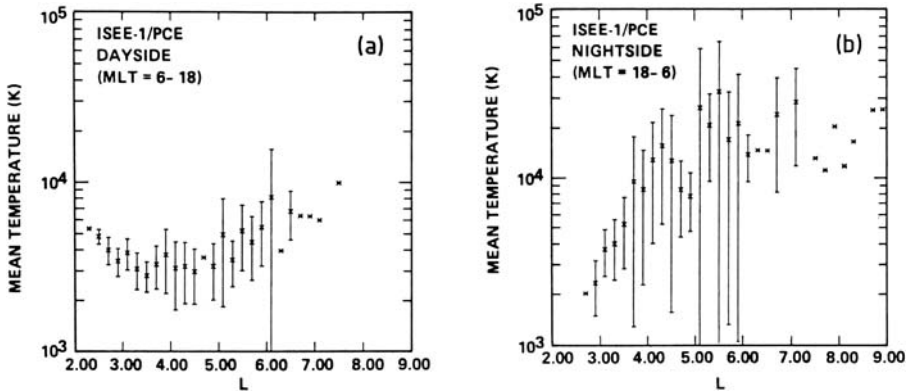
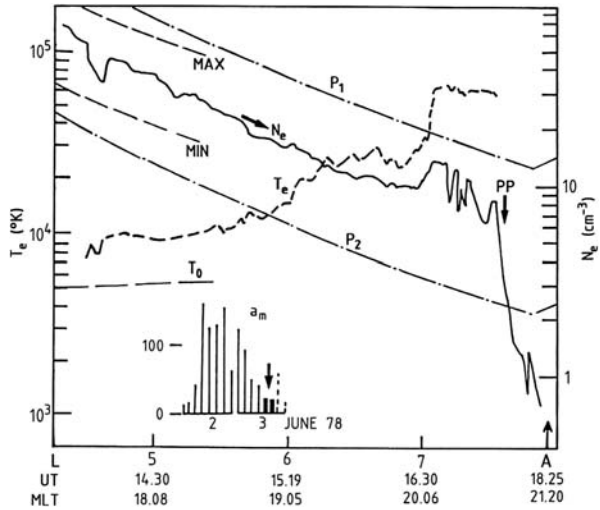


**Fig. 8** Mean hydrogen temperature as a function of  $L$  for (a) the dayside and (b) the nightside plasmasphere, from observations by ISEE 1. (Adapted from Comfort 1986)

gradient for  $L < 3$ , an effect that remains unexplained. For  $L > 4$ , the temperatures are higher at night (Comfort 1986).

Figure 9 shows four typical density profiles (Carpenter and Anderson 1992) obtained by the Passive Wave Instrument (PWI) on ISEE 1. The crossing on day 215 shows a well-defined plasmapause, whereas the crossings on days 217 and 219 show a recovering plasmasphere with a less pronounced plasmapause. The last crossing, on day 224, after some geomagnetic activity, shows a well-defined plasmapause again. These observations illustrate the cyclic pattern of erosion during disturbed periods and recovery thereafter. DE 1 and 2, launched in 1981, helped to define categories of density profiles (Horwitz et al. 1990). For example, Fig. 10 presents different  $H^+$  and  $He^+$  density profiles, some of which feature non-monotonic variations. To which three-dimensional structures these profiles were related, could not be resolved at that time because of the single-point nature of the measurements.

During the later 1980s and the 1990s new missions brought increased observing power. Some highlights include AKEBONO measurements of the parallel drift velocities of various

**Fig. 9** Electron density profiles as a function of  $L$  for 4 plasmasphere crossings obtained with the Passive Wave Instrument (PWI) on ISEE 1. (From Carpenter and Anderson 1992)

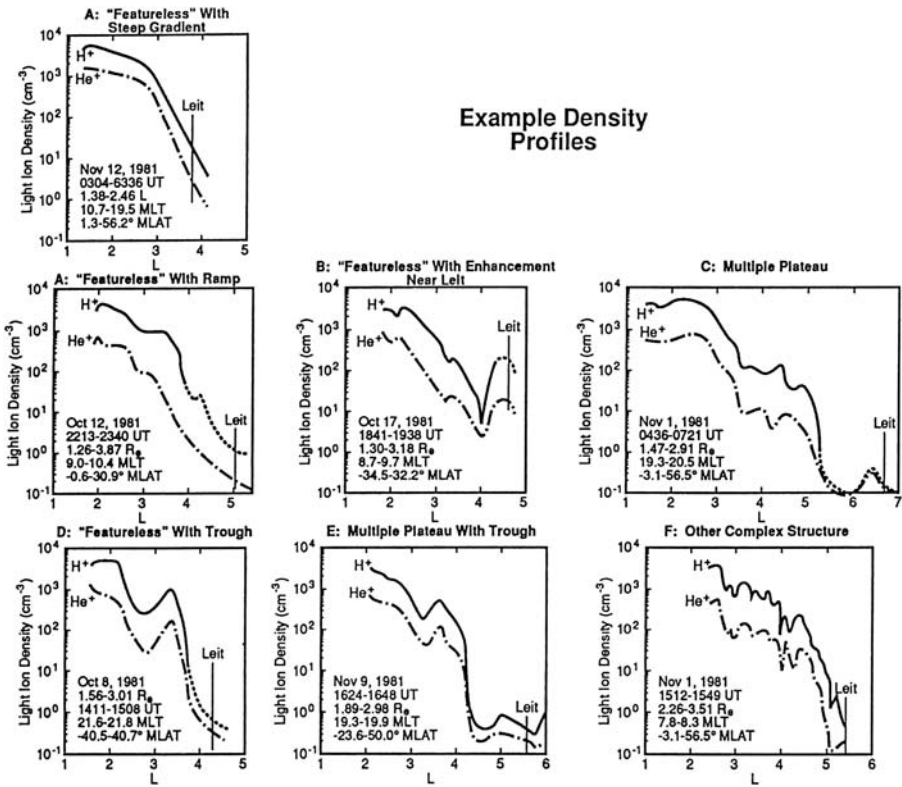
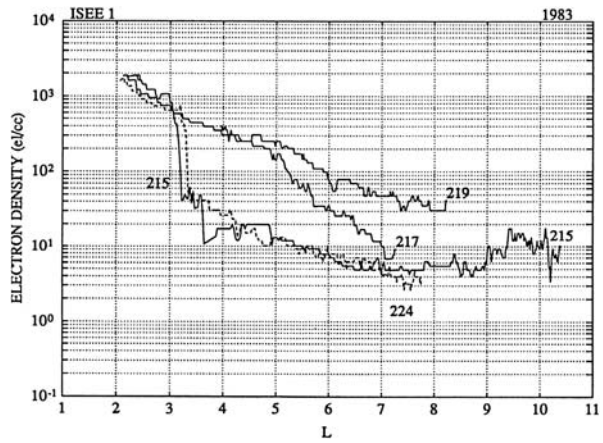


**Fig. 10** Classification of hydrogen ( $H^+$ ) and helium ( $He^+$ ) density profiles based on DE 1 observations. (From Horwitz et al. 1990)

ions (Watanabe et al. 1992) and of geoelectric field variations with latitude at 10,000 km altitude (Anderson et al. 2001). The Russian INTERCOSMOS 24 and 25 satellites provided information on plasma composition (Afonin et al. 1994) and new results were obtained

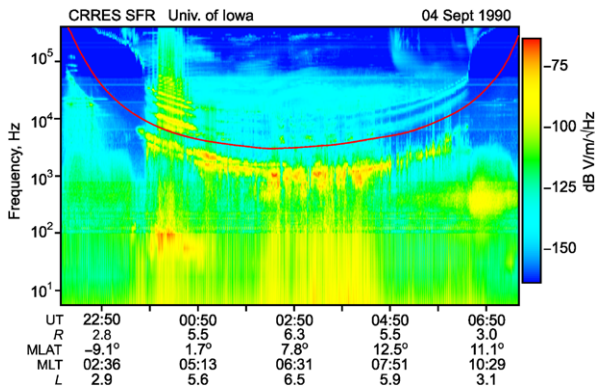


**Fig. 11** CRRES sweep frequency receiver data for an orbit on September 4, 1990, with approaches to perigee at far left and right and apogee at  $\sim 06:30$  MLT. The local gyrofrequency is shown by the *curving line*. The plasmasphere is outlined at upper left and right by the upper hybrid noise band. A noise enhancement associated with the equator appears near 23:30 UT. Below the gyrofrequency, a band of VLF chorus extends throughout the region outside the plasmasphere. In that same region and above the gyrofrequency are several bands of cyclotron harmonic waves, above which there is trapped continuum radiation. Above and to the right are two Type III solar noise bursts, while to the right and inside the plasmasphere there is plasmaspheric hiss near 500 Hz. (Courtesy of R.R. Anderson)

from COSMOS-900 on thermal coupling between the plasmasphere and the ionosphere in the plasmasphere boundary layer (Afonin et al. 1997). The CRRES spacecraft, launched in 1990, proved to be an excellent resource for study of cold electron density profiles both inside and outside the plasmopause (Moldwin et al. 2002) and for detecting complex density structure that develop near the plasmopause (LeDocq et al. 1994). CRRES provided data on electric fields and their enhancements in the dusk sector during periods of enhanced convection (Burke et al. 1998). It also contributed to the study of waves in the plasmasphere by detecting many different kinds of waves over a wide frequency range (see Fig. 11 and, e.g., Anderson 1994). Yet all these missions, however sophisticated their instruments, suffered from the fact that the measurements were made locally. Any measured time variations could be both due to spatial or temporal variations, or both. A partial remedy was offered by the Los Alamos geosynchronous satellites, located at different longitudes, which offered a (relatively crude) way of distinguishing between temporal and longitudinal variations. In particular, the plasma analyzers on these spacecraft provided new information on irregular density structure and the properties of plasmaspheric plumes as those have recently come to be identified (Moldwin et al. 1994; Thomsen et al. 1998), although their measurements were constrained to the radial distance corresponding to geosynchronous orbit, which is often well outside the plasmasphere.

The need to be able to resolve space and time variations with in situ data was recognized and led to the INTERBALL mission, which consisted of two pairs of spacecraft: INTERBALL 1/MAGION 4 and INTERBALL 2/MAGION 5, launched in 1995 and 1996. While testing a number of multipoint data interpretation techniques for the magnetospheric boundary, the multi-spacecraft aspect was not really exploited for plasmaspheric research. Nevertheless, this mission showed that the ion temperature in the plasmasphere increases with MLT from the post-midnight to pre-noon sector in the innermost part of the dawn plasmasphere (Kotova et al. 2008). In the outermost plasmasphere, however, no temperature dependence with MLT was observed. MAGION 2, a subsatellite of INTERCOSMOS 24 (ACTIVNY), found thermal  $O^{++}$  density peaks within the plasmasphere (Smilauer et al. 1996).

### 2.3 Radio Probing from Ground and Space

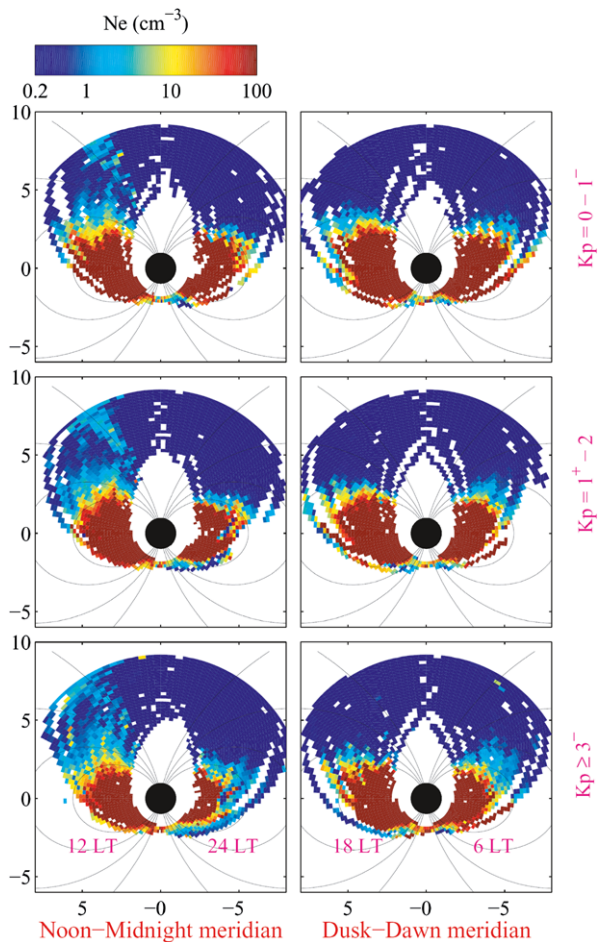
Both ground- and spacecraft-based radio probing have evolved considerably. Much of the ground-based probing work prior to the IMAGE and CLUSTER missions is summarized by Lemaire and Gringauz (1998). While radio probing originally began with the study of whistler-mode waves, other types of emission have gained attention more recently. Useful reviews of whistler-mode waves as diagnostic tools are the papers by Gurnett and Inan (1988), Sazhin et al. (1992), and Hayakawa (1995). The volume by Labelle and Treumann (2006) reviews active probing in space using the Z-mode (Benson et al. 2006), kilometeric continuum radiation (Hashimoto et al. 2006), and the influence of plasma density irregularities on whistler-mode propagation (Sonwalkar 2006).

Magnetospheric reflection, in which whistler-mode waves propagate back and forth across the equator after reflecting near locations where the local LHR frequency matches the frequency of the wave, is of considerable geophysical importance (Kimura 1966; Shklyar and Jiříček 2000; Bortnik et al. 2003). Non-ducted propagation of whistler-mode waves and the occurrence of whistler-mode emissions in space were discussed by Smith and Angerami (1968), Matsumoto and Kimura (1971), Sonwalkar (1995), and others. Plasmaspheric hiss has been studied extensively (Thorne et al. 1973; Hayakawa and Sazhin 1992). Important theoretical work was accomplished on the interplay of waves and the hot plasmas of the radiation belts (Kennel and Petschek 1966) and on the possible origin of continuum radiation in a mode conversion process at the plasmasphere boundary layer (Jones 1982). The introduction of the concept of a wave distribution function (Storey and Lefeuvre 1979, 1980) heralded the beginning of efforts to track waves observed on spacecraft to their regions of origin. A lot of work was devoted to the study of non-linear whistler-mode wave–particle interactions using a ground-based transmitter in Antarctica (Helliwell and Katsufakis 1974; Paschal and Helliwell 1984; Helliwell 1988), supported by theoretical modeling (e.g., Nunn 1974; Omura and Matsumoto 1982; Gibby et al. 2008). The loss of radiation belt particles through scattering by whistler-mode waves has been studied by, e.g., Inan et al. (1978), Burgess and Inan (1993), and Abel and Thorne (1994).

The importance of radio measurements is illustrated by the results of the POLAR mission. Launched in 1996, this spacecraft followed CRRES, ISEE 1, and others (Anderson 1994), by providing excellent surveys of wave activity over a wide range of frequencies. At this stage, radio instruments as well as the corresponding data interpretation had evolved into true remote sensing techniques. For instance, POLAR data allowed Laakso et al. (2002) to construct meridional cross-sections of the average electron density distribution in the plasmasphere, and showed that the dawn–dusk asymmetry increases with  $K_p$ , presumably due to strong motion of the dawnside plasmopause (Fig. 12). Measurements of local plasma emissions lead to very precise determinations of plasma densities, and have resulted in empirical plasmasphere and plasmatrough density models using the POLAR dataset (Denton et al. 2002).

Currently, global positioning system (GPS) signal propagation delays through the ionosphere are being analyzed to infer ionospheric total electron content (TEC). TEC provides information on the state of the plasmasphere as the ionosphere can be regarded as the downward prolongation of plasmaspheric flux tubes. For instance, so-called “tongues of ionization” observed in the ionosphere are probably the signature of plasmaspheric plumes (Foster et al. 2002). Space-to-space propagation measurements allow one to reconstruct the ionosphere and low-altitude plasmasphere by inversion of the propagation delays (e.g., Heise et al. 2005; Stankov et al. 2005).

**Fig. 12** Average electron density in two meridional planes derived from POLAR Electric Field Instrument (EFI) data between 1 April 1996 and 31 December 1999. The *left panels* are for the noon-midnight meridian, and the *right panels* are for the dusk-dawn meridian. The panels from top to bottom are for three different  $K_p$  ranges. (From Laakso et al. 2002)



### 2.4 Theoretical Understanding

Early attempts tried to interpret the plasmapause phenomenon in terms of a separatrix between two flow regimes, or as a region of finite but occasionally steep gradients that was subject to plasma instabilities. Perhaps the boundary was something in between, patchy because of a combination of unsteadiness in the large-scale convection and instabilities on smaller scales. These questions have prompted theoretical studies of the stability of the plasmapause profile (e.g., Richmond 1973; Lemaire 1975), as well as the development of magnetohydrodynamics-based and kinetic models of the plasmasphere and its erosion and recovery (see Pierrard et al. 2008, this issue). Further progress toward understanding the erosion processes would clearly depend upon the ability of the observations to cover larger regions of the plasmasphere boundary so as to elucidate its topology. Typical examples were the “detached plasma elements”, which in current global views are not seen to be physically detached from the main plasmasphere.

Another fundamental, but notoriously difficult problem was the study of plasmasphere refilling. With single-spacecraft measurements it was impossible to obtain solid information on the density profiles along field lines. Such information was needed to be able to establish

the rate of refilling, and how refilling changes with time (see Darrouzet et al. 2008, this issue).

The concept of shielding of the inner magnetosphere was relatively well established, but needed observational support concerning the meso-scale electric field distributions in the inner magnetosphere. This was particularly true for understanding the role of the subauroral polarization stream electric fields and the associated subauroral ion drift, which is a manifestation of the interaction of the cross-tail electric field and the plasma sheet on one hand and the corotation electric field in the plasmasphere on the other hand (see also Matsui et al. 2008, this issue).

Progress on these subjects stalled because of a lack of global-scale observations, coupled with slowness on the part of the magnetospheric physics community to recognize the geophysical importance of what is now called the plasma boundary layer (Carpenter and Lemaire 2004). With CLUSTER and IMAGE and their new observation strategies, and thanks to appropriate data analysis techniques, a new chapter has opened on both the experimental and interpretive sides of this problem.

### 3 The Quest for a More Global View

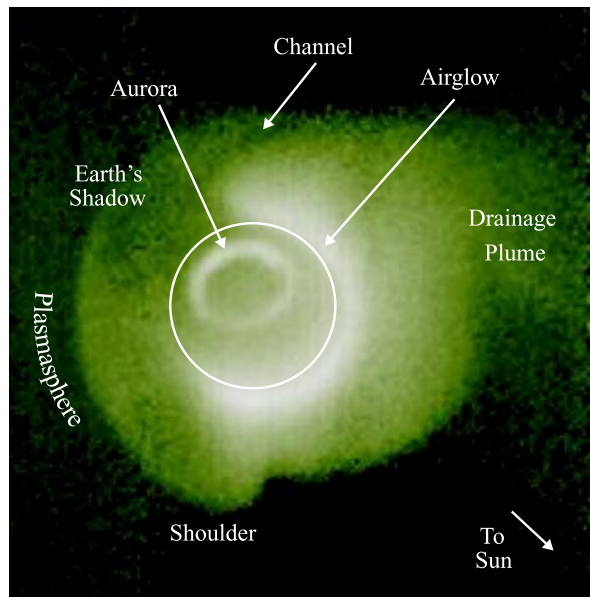
There are two ways to obtain non-local information: either by making in situ observations at a number of different points, which requires multi-spacecraft constellations such as CLUSTER, or by developing remote sensing techniques that are able to detect a proxy for the desired plasma information from a distance, which is the idea behind the IMAGE mission. Both missions were launched in 2000. IMAGE stopped operations at the end of 2005, while the CLUSTER mission has been extended to the end of 2009, at least.

#### 3.1 The Rationale of Global Imaging: IMAGE/EUV Observations

IMAGE's Extreme UltraViolet (EUV) imager (Sandel et al. 2000) observed sunlight resonantly scattered off  $\text{He}^+$  ions, producing an emission at 30.4 nm. The plasmasphere contributes much to this emission as it is one of the most dense regions of the magnetosphere, with  $\text{He}^+$  densities up to thousands of particles per  $\text{cm}^3$ . Useful images are obtained through long exposure times and long line of sight contributions through the optically thin plasma medium. The high latitude initial apogee of the IMAGE orbit ( $8.2 R_E$ ) offered an optimum vantage point for observing the azimuthal structure and dynamics of the plasmasphere. The exposure time was limited because of spacecraft motion. Limitations on the telemetry also prohibited a fast imaging cadence; EUV provided an image every 10 minutes. The instrument has a wide field of view. It consists of three cameras, each with an opening angle of  $30^\circ$  and together covering a fan-shaped field of  $84^\circ \times 30^\circ$ .

Figure 13 shows a typical EUV image taken near apogee. It shows the ultraviolet glow of the dayside upper atmosphere on the sunlit side of the Earth, the auroral oval encircling the northern magnetic pole in the upper atmosphere, and the plasmasphere as a glowing halo around the Earth. Interpreting such images is not trivial since EUV images record line-of-sight integrated intensities. As EUV looks down on Earth from a vantage point that is not exactly over the pole, geometric corrections must be performed. Actual densities can be obtained by means of image inversion techniques, although simpler heuristics also work well, as discussed in Sect. 4.1. Rescaling the  $\text{He}^+$  densities into total densities depends on assumptions concerning the  $\text{He}^+$  relative abundance;  $\text{He}^+$  density is about 15% of the  $\text{H}^+$  abundance in the plasmasphere (Craven et al. 1997). The sensitivity of the instrument corresponds to a lower limit of about  $40 \text{ cm}^{-3}$  equatorial plasma density (Goldstein et al. 2003c);

**Fig. 13** EUV image of the plasmasphere at 30.4 nm at 07:34 UT on 24 May 2000, at a range of  $6.0 R_E$  and a magnetic latitude of  $73^\circ$  N. The Sun is to the lower right, and Earth's shadow extends through the plasmasphere toward the upper left. The *bright ring* near the center is an aurora. The *white circle* gives the size of the Earth. Several plasmaspheric structures often visible in such images are indicated. (Adapted from Sandel et al. 2003)



the outer layers of the plasmasphere therefore cannot be seen completely. The spatial resolution is about  $0.1 R_E$  when IMAGE is at apogee (Sandel et al. 2000). Other complications arise from the effects of the Earth's shadow, of auroral ultraviolet emission, and of the airglow on the EUV images. Several instrumental issues have to be dealt with, such as image contamination, matching of the data produced by the three detector heads, and aging of the detectors. In spite of these complications, EUV images are a treasure trove of plasmaspheric structures. They have led to a new morphological nomenclature (Sandel et al. 2003, see also <http://image.gsfc.nasa.gov/poetry/discoveries/N47big.jpg>) for various types of spatial structures (Darrouzet et al. 2008, this issue).

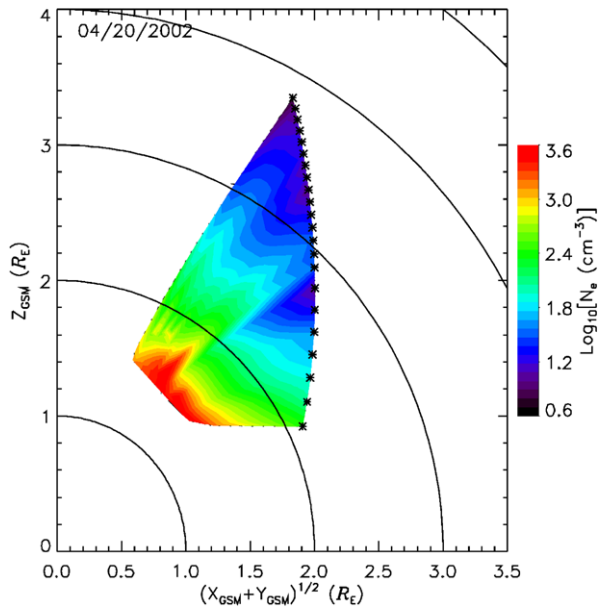
The IMAGE spacecraft also carried other global imaging instruments, the High, Medium, and Low Energy Neutral Atom (HENA/MENA/LENA) imagers (Mitchell et al. 2000; Pollock et al. 2000; Moore et al. 2000). Energetic neutral atom imagers address the distribution of higher-energy particles (10–500 keV/nucleon, 1–70 keV/nucleon, and 10–500 eV/nucleon, respectively). These imagers help to shed light on the dynamical interaction in the coupled ring current–plasmasphere system (Williams et al. 1992; Brandt et al. 2002; Gurgiolo et al. 2005).

### 3.2 Radio Observations in Space with IMAGE/RPI

The Radio Plasma Imager (RPI) on IMAGE operated in the frequency range from 3 kHz to 3 MHz using three orthogonal antennas, two 500 m long dipoles in the spin plane, and a 20 m dipole along the spin axis. The design and measurement characteristics of RPI have been described in detail by Reinisch et al. (2000).

The RPI instrument alternated between making passive electric field measurements and active radio sounding measurements. Each of those modes of operation are analyzed and displayed differently. In active sounding mode, the RPI emitted coded signals and listened for reflected echoes. The received echoes are plotted in a “plasmagram” with the analysis software known as BinBrowser (Galkin et al. 2004a, 2004b). A plasmagram is a color-coded

**Fig. 14** Two-dimensional electron density image projected into the  $Z_{\text{GSM}}-r$  plane, where  $r^2 = X_{\text{GSM}}^2 + Y_{\text{GSM}}^2$  from RPI measurements on 20 April 2002 when IMAGE flew from the polar cap toward the plasmasphere at  $\sim 12$  MLT. (Courtesy of J. Tu)



display of the signal amplitude as a function of frequency and echo delay time. The echo delay time is usually represented by the so-called virtual range, i.e., half the delay time multiplied with speed of light in free space. If the actual signal propagation speed does not differ much from the speed of light in free space, the virtual range gives an idea of the distance at which the signal was reflected.

When the RPI was sounding inside or close to the plasmapause, there were often discrete echoes forming traces with virtual ranges of up to  $7 R_E$  when echoes from the conjugate hemisphere were received. Outside the plasmasphere, the RPI acquired discrete echo traces with virtual ranges of  $3-4 R_E$ . These traces appear to represent signals that were reflected remotely and propagated along the magnetic field line (Reinisch et al. 2001; Green and Reinisch 2003; Fung and Green 2005). By scaling the traces, i.e., recording the frequency and virtual range pairs, an electron density distribution along the magnetic field line that intersects the spacecraft can be derived (Huang et al. 2004). How trace information can be translated into density profiles will be discussed briefly in Sect. 4.2.1. The measurement of a single field-aligned density profile takes typically 1 minute. Multiple density profiles were obtained along the IMAGE orbit and can be used to construct a two-dimensional electron density image covering a large area of the inner magnetosphere. Figure 14 shows such an image that was constructed from RPI measurements obtained as the IMAGE spacecraft flew over the polar cap, crossed the dayside cusp/auroral oval, and entered the plasmasphere at lower latitudes.

In passive measurement mode, the RPI monitored the natural plasma wave environment around the satellite. Those natural plasma wave signals are displayed in conventional frequency-time electric field spectrograms or dynamic spectra (e.g., Green and Reinisch 2003). Typical features on an RPI dynamic spectrogram are a narrow upper hybrid resonance (UHR) noise band, kilometric continuum (KC) radiation, and the non-thermal continuum (NTC) radiation (see Masson et al. 2008, this issue). The lower cutoff frequencies of the UHR band and the NTC radiation provide an estimate of the electron plasma frequency  $f_{pe}$  or, equivalently, electron density  $n_e \propto f_{pe}^2$  (e.g., Mosier et al. 1973; Shaw and Gurnett 1980;

Benson et al. 2004). The RPI in its passive mode therefore can be used much like earlier wave instruments (e.g., the Plasma Wave Instrument, PWI, on POLAR) to study the plasma-pause, plasmaspheric troughs, and plumes. The techniques underlying that kind of analysis are discussed in Sect. 4.2.2.

### 3.3 Disentangling Spatial and Temporal Variability with CLUSTER

The four CLUSTER spacecraft (C1, C2, C3 and C4) fly in a tetrahedral configuration along similar inclined orbits with a perigee of about  $4 R_E$ . They cross the outer plasmasphere from the southern to the northern hemisphere every 57 hours. Each CLUSTER satellite contains 11 identical instruments. Five of them are of particular relevance to the study of the plasmasphere:

- The magnetic field measurements by the FluxGate Magnetometer (FGM) (Balogh et al. 2001) are very accurate, with a broad dynamic range. The weakest fields are measured with an error below 0.1 nT and a (cross-)calibration down to the same level. These data are therefore well suited for the computation of gradients. The sampling rate can be as high as 67 Hz, but spin-averaged (4 s) data are usually sufficient for plasmaspheric studies.
- The CLUSTER Ion Spectrometry (CIS) experiment (Rème et al. 2001) consists of two detectors, CODIF and HIA. Most useful in the plasmasphere is CODIF in RPA mode, in which the detector potential is biased relative to the spacecraft environment so as to repel photo-electrons and to facilitate capture of the cold (a few eV) ions, but even then a fraction of the cold ion distribution may be missed. Nevertheless, useful data about density variations, composition, and plasma flow can be obtained (see also Darrouzet et al. 2008, this issue). Cross-calibration is difficult since the environment of each spacecraft is different. Note that the PEACE electron spectrometers usually are not operating in the plasmasphere because it is hard to separate plasmasphere electrons from the photo-electron cloud.
- The wave sounder (WHISPER, Waves of High frequency and Sounder for Probing Electron density by Relaxation) (Décréau et al. 2001) observes plasma waves. In its passive mode, the receiver monitors the natural plasma emissions in the frequency band 2–80 kHz. In its active mode, the sounder analyses the pattern of resonances triggered in the medium by a radio pulse. Various types of waves have been observed in the plasmasphere (see Masson et al. 2008, this issue). The resonance signatures in both modes lead to an independent estimation of  $f_{pe}$ , which provides a well-calibrated measurement of  $n_e$ . Because of WHISPER's frequency limits, the method is applicable for densities between 0.05 and  $80 \text{ cm}^{-3}$ .
- The Electric Field and Wave (EFW) experiment (Gustafsson et al. 2001) measures the electric potentials of the antenna probes (mounted on two pairs of extended boom wires, with a distance of  $\sim 88$  m between each pair of probes) and of the spacecraft body. The instrument provides the spin-plane electric field components, which is interesting for the study of the plasmaspheric convection electric field (see Matsui et al. 2008, this issue), as well as the spacecraft potential. Using a non-linear empirical relation, which depends on the plasma regime, the electron density can be estimated from this potential (Pedersen 1995; Laakso and Pedersen 1998; Moullard et al. 2002; Pedersen et al. 2008). For each plasmasphere traversal the EFW measurements can be calibrated against the WHISPER-derived densities (Pedersen et al. 2001) wherever the density is below  $80 \text{ cm}^{-3}$ . Unfortunately, extrapolation of the calibration relation to higher densities is not justified.

- The Electron Drift Instrument (EDI) (Paschmann et al. 2001) emits a steerable beam of electrons and detects when it returns to the spacecraft. A controller commands the electron guns to track the return beam continuously. The convection electric field can be derived from the steering signal. This technique works well when there is no strong time variability. EDI returns excellent results in the plasmasphere. EDI and EFW measurements can be combined to provide a comprehensive electric field dataset (see Reinisch et al. 2008, this issue).

Multi-spacecraft missions like CLUSTER require appropriate data analysis techniques to exploit the multipoint nature of the observations. A nice review of multi-point methods can be found in the books edited by Paschmann and Daly (1998) and Paschmann and Daly (2008). Experiences with these methods in the study of the outer magnetosphere are reported by Paschmann et al. (2005). Further development of such methods is an ongoing effort.

Single-spacecraft measurements do not allow for a determination of whether observed variations are due to spatial or temporal changes. The idea behind the CLUSTER mission was to launch four spacecraft into nearby orbits, so that the variations in space and time can be sorted out. Simultaneous measurements at four non-coplanar points allow one to evaluate the spatial gradient (see Sects. 4.3 and 4.4). In order to work properly, the spacecraft must all be embedded in the gradient structure at the same time (the homogeneity condition). The spacecraft separations have therefore been adapted in the course of the mission, varying between 100 km and 10000 km: small separations to study the bow shock and the magnetopause, and larger separations to study the tail. Some difficulties with the homogeneity condition can be overcome by making assumptions about the objects that are being sampled. For instance, if the plasmopause is a locally planar interface, one can use the positions and the relative times at which the spacecraft cross the plasmopause to infer its orientation and speed, without requiring all spacecraft to be inside the plasmopause at the same time (see Sect. 4.5).

## 4 New Data Analysis Tools

Both the IMAGE and CLUSTER missions pioneer new observational paradigms and therefore require new data analysis techniques. Without the pretension of being complete, we review a number of examples of such methods that are relevant for the study of the plasmasphere so as to give an idea of the flavour of these techniques.

### 4.1 Analysis of Global Images

In this section, we first give an overview of different techniques that have been used for IMAGE/EUV image analysis. We then focus on one technique in more depth to illustrate some of the issues that must be addressed.

#### 4.1.1 Overview of Methods

Analyzing EUV images typically involves one or more of the following processing steps.

*Removal of Noise and Instrument Artifacts* Because of the constraints on image acquisition time, detector sensitivity, and the low densities in the outer plasmasphere, and despite the integrated nature of the images along the line of sight, EUV's images can be noisy. An obvious way to improve the signal-to-noise ratio is by accumulating subsequent images

(e.g., Burch et al. 2004). Smoothing and/or binning of the image can reduce noise at the expense of a loss in spatial resolution. Specific noise reduction techniques have been used to suppress random small-level density fluctuations that might hamper correlating subsequent images (Gallagher and Adrian 2007). Binning has been used by Darrouzet et al. (2006a) to detect plasmaspheric plume tips down to relatively low densities. Gurgiolo et al. (2005) use a despeckling algorithm to remove isolated active pixel clusters, which can be regarded as an intelligent form of binning.

Subtraction of the image background largely eliminates the adverse effects of stray-light in the EUV instrument and facilitates further image processing (Gurgiolo et al. 2005; Gallagher and Adrian 2007; Galvan et al. 2008). A quite sophisticated approach is the use of data quality flags to eliminate the Earth's shadow region, the auroral emission, and the seams between the fields-of-view of the three EUV cameras from the analysis (Galvan et al. 2008). Not doing so results in erroneous contributions to the solution in the subsequent image inversion process (Gurgiolo et al. 2005).

*Photometric Calibration* Intensity variations of the solar flux must be taken into account. A proxy for this flux can be obtained from SOHO instruments (Gallagher et al. 2005; Galvan et al. 2008). The flux dependence is especially important if precise photometric calibration is needed, in particular when one wants to compare several EUV images, or if one wants to compare them to data acquired in situ. Examples include studies of plasmaspheric flux tube content (Sandel and Denton 2007; Galvan et al. 2008) or motion of low-contrast plasmaspheric features (Gallagher et al. 2005; Galvan et al. 2008).

*Three-Dimensional Inversion and Projection on the SM Equatorial Plane* Images are taken from a specific vantage point, often high above the pole. Because of the varying distance from Earth and the changing viewing direction it is necessary to properly account for the observation geometry.

A full inversion of a plasmaspheric image or of a set of successive images (Williams et al. 1992; Roelof and Skinner 2000; Gurgiolo et al. 2005) should include all relevant observations, as well as the known magnetic field geometry and the physical mechanisms of emission and detection of the radiation. In particular, inversion can benefit from a good field-aligned density model. Depending on the available data, parts of the solution may not be well-constrained, so that regularization assumptions enforcing a certain smoothness are needed. Noise adversely affects the inversion process. The inversion produces the complete three-dimensional density distribution. Inversion is a computationally expensive iterative process; it has therefore been used especially in situations where precise plasmopause positions are required (e.g., Larsen et al. 2007). Note that similar inversion techniques can be applied to the HENA, MENA, and LENA images, although in that case assumptions concerning the isotropy and the energy spectra of the particles have to be made to convert the differential number flux into velocity space distribution densities, which results in the actual densities after integration (Gurgiolo et al. 2005).

If an image is obtained from more or less straight above the pole, the equatorial projection of the plasmopause is simply the plasmasphere silhouette determined as an isophote (e.g., Garcia et al. 2003; Goldstein et al. 2003b). For other viewing directions one can use the "edge algorithm" to compute the equatorial projection of the plasmopause from the viewing geometry and the plasmasphere silhouette in the acquired image, without the need for a full inversion (Roelof and Skinner 2000). The correctness of this approach can be proven under certain simplifying assumptions. A detailed evaluation by Wang et al. (2007) indicates that the algorithm suffers from a number of problems, such as the non-uniqueness of

the radial plasmopause position when a plume is present, and difficulties with certain atypical projection geometries and with image discretization effects. These authors propose a “revised edge algorithm” that addresses some of these issues. Yet another alternative is the minimum- $L$  algorithm (e.g., Gallagher et al. 2005). While not so precise as the edge algorithm, this technique has been shown to be sufficiently accurate in practice, with errors on the radial plasmopause position of a few percent at most, especially if the plasmasphere is observed from a vantage point high above the pole (Wang et al. 2007). The technique is also very general and robust. It is used very often (Brandt et al. 2002; Sandel et al. 2003; Spasojević et al. 2003; Garcia et al. 2003; Goldstein et al. 2003c, 2004; Adrian et al. 2004; Burch et al. 2004; Gallagher and Adrian 2007; Sandel and Denton 2007; Galvan et al. 2008), in part because it can map each image pixel onto the equatorial plane while at the same time converting the line-of-sight integrated density to a pseudo-density by dividing it by an estimate of the line-of-sight distance that contributes most to the intensity in each viewing direction (for more details, see Gallagher et al. 2005). In doing so, this pseudo-density is a fair approximation of the equatorial density that would be obtained from a full inversion. The same rationale is followed by Sandel and Denton (2007) to combine the minimum- $L$  algorithm with the effective pathlengths along the lines of sight to convert the time derivatives of  $\text{He}^+$  column density into equivalent volume refilling rates at the equator.

*Density Calibration* A proper density calibration is needed to relate the inferred  $\text{He}^+$  densities to the total density. People often rely on a constant  $\text{He}^+$  abundance ratio from an earlier statistical study (Craven et al. 1997) to obtain total densities. Such a rescaling, however, should be performed with caution as the actual  $\text{He}^+$  abundance ratio can vary throughout the plasmasphere. This can be an issue, for instance, in studies of refilling (Sandel and Denton 2007). The  $\text{He}^+$  distribution resembles the overall total plasma distribution, as has been confirmed by the high correlation between plasmopause and plume positions obtained from in situ IMAGE/RPI total densities and from IMAGE/EUV  $\text{He}^+$  densities (Garcia et al. 2003; Goldstein et al. 2003c; Moldwin et al. 2003). More detailed studies suggest an enhancement of the heavy ion populations in the inner plasmatrough during active refilling periods; this enhancement, however, is ascribed to  $\text{O}^+$  rather than  $\text{He}^+$  (Dent et al. 2006; Grew et al. 2007).

*Comparison of Successive Images* EUV movies of images at a 10 minute cadence enable studies of the dynamics of plasmasphere structure. Especially when IMAGE had its apogee high above the North Pole, it was able to record long sequences of images.

The time evolution of structures in the plasmasphere can be followed by visual inspection of a movie. Examples include tracking the position of plasmaspheric notches or plumes in order to derive the effective corotation speed (Garcia et al. 2003; Sandel et al. 2003; Spasojević et al. 2003; Gallagher et al. 2005), monitoring the shape of shoulders, notches, plumes and channels to see how they develop (Spasojević et al. 2003; Gallagher et al. 2005), or following the inward and outward motion of the plasmopause at a fixed MLT to monitor plasmasphere compression/erosion and expansion/refilling by relating this motion to the dawn-dusk electric field and its solar wind driver (Goldstein et al. 2003a, 2007). In general, following cold plasma structures reveals information about the magnetospheric convection electric field (Goldstein et al. 2003b, 2005). Visual inspection of EUV movies may also be guided by models (see Pierrard et al. 2008, this issue).

Automated cross-correlation of successive images is particularly useful when analyzing large datasets and/or to avoid subjective effects in feature identification. Burch et al. (2004)

analyze the brightness curve along an annulus to identify the position of notches, while Gallagher et al. (2005) use least-squares fits to describe notch geometry to assist in obtaining more precise notch positions; both studies do this in consecutive images to obtain notch drift velocities and to gain insight as to why sub-corotation is usually observed. Gallagher and Adrian (2007) correlate subsequent images to infer the two-dimensional  $\text{He}^+$  flow in the magnetic equatorial plane, from which the global and mesoscale electric fields can be determined. Another highly automated technique is that of Galvan et al. (2008): They use the cross-correlation of the densities in an annulus, as observed in subsequent images, to infer the corotation speed. This allows them to identify the diurnal plasmaspheric density variations that are recorded as one follows individual plasma elements. The up/down flows due to the exchange of plasma between the ionosphere and the plasmasphere throughout day and night can then be computed from these density variations.

*Data Accumulation* It is always possible to use data accumulation to suppress statistical uncertainties. In their study of refilling rates, Sandel and Denton (2007) use azimuthal binning of their pre-processed data to obtain column abundances over concentric rings at successive  $L$  values. To improve their statistics even more, such data are summed over a number of orbits. Galvan et al. (2008) accumulate their set of density changes in flux tubes as a function of time, which are derived from low-contrast changes in the EUV image intensities collected during an orbit, by considering a large set of 128 orbits to maximize the statistical significance of their results and to obtain a complete picture of the diurnal density variations.

*Visualization Aids* In addition to the specific analysis methods discussed above, various techniques have been used to cope with the high dynamic range of the images, such as: the use of contrast enhancement techniques, rendering the images in false color, using intensity scales proportional to the square root or the logarithm of the image intensity, plotting radial gradients of the data (Sandel et al. 2003) or visualizing the data with various image projection formats such as polar plots or MLT- $L$  diagrams (e.g., Gallagher et al. 2005). Such visualization techniques can sometimes reveal surprising phenomena. For instance, contrast enhancement by differencing of images after a proper amount of rotation ("residue images") has revealed radial brightness variations corresponding to what might be interpreted as a standing global magnetospheric wave pattern (Adrian et al. 2004).

*Correlation with Data from Other Spacecraft or Ground Stations* An analysis can always benefit from additional information from other sources. In particular, every analysis of plasmasphere data has to take into account the role of geomagnetic activity, for instance, expressed in terms of the  $K_p$  index deduced from ground observations. An alternative is to study the relationship between the plasmasphere and the solar wind parameters directly. An attempt in this direction has been made by Larsen et al. (2007), who have used a multiple regression analysis to relate the average plasmopause position derived from EUV image inversion to ACE solar wind parameters. This analysis shows that the time-delayed interplanetary magnetic field  $B_z$ , its clock angle  $\theta$ , and the merging proxy  $\phi = vB \sin^2(\theta/2)$ , where  $v$  and  $B$  denote solar wind speed and field magnitude, are the dominant controlling parameters. The time delays are found to be around 200 minutes. Although statistical in nature, and although the MLT-dependence of the plasmopause is not taken into account, this regression analysis gives indications about the physical processes involved in the response of the inner magnetosphere to the solar wind driver. Goldstein et al. (2003a) have studied the direct correspondence between the dawn-dusk electric field computed from time-delayed

ACE data and the plasmaspheric electric field inferred from plasmopause motion in EUV movies, as an illustration of the physical mechanism of plasmaspheric erosion.

Various other correlative studies have been performed with EUV data. EUV densities have been compared to in situ measurements of plasmaspheric densities and plume densities by IMAGE/RPI (Reinisch et al. 2004), by CLUSTER (Darrrouzet et al. 2006a), and by the LANL satellites (Moldwin et al. 2003; Goldstein et al. 2004). EUV data have been correlated to ground magnetometer data and RPI data to infer composition (Dent et al. 2006; Grew et al. 2007). Notch drift velocities inferred from the EUV images have been compared with DMSP ionospheric drifts (Burch et al. 2004; Gallagher et al. 2005) to understand differential rotation. Combined analysis of EUV and HENA and MENA data has contributed to studies of the ring current–plasmasphere interaction and its role in subauroral ionospheric heating (Brandt et al. 2002; Gurgiolo et al. 2005). Variations in EUV-derived plasmopause positions have been related to auroral features visible in IMAGE/FUV auroral keograms (Goldstein et al. 2007). EUV densities have also been compared to GPS-TEC ionospheric density maps and DMSP ionospheric densities and drifts to study the overlap between the subauroral polarization stream and plasmaspheric plumes (Foster et al. 2007).

#### 4.1.2 Example: A Technique for Determining Plasmaspheric Drifts

We describe the technique proposed by Gallagher and Adrian (2007) to determine plasmaspheric convection in more detail. The basic premise is that EUV detects a lot of structure that can be recognized in subsequent images. The technique is based on matching features from one image to the next by cross-correlation analysis. The images are photometrically calibrated and are projected to the equatorial plane first, which is done with the minimum- $L$  technique. Figure 15 displays the pseudo-density projected in the solar magnetic equatorial plane for two successive 10-minute integrated images, centered at 05:45 UT and 05:55 UT on 10 July 2000, using a logarithmic gray-scale to represent the pseudo-densities. A kernel representing a portion of the first image is differenced with the same sized portion of the subsequent image to determine the quality of correspondence. Cross-correlation coefficients are calculated across a range of subimages until the best match is found or until it is determined that no match of sufficient quality can be found. Since any drift must be finite in speed, the number of locations at which the cross-correlations must be computed can be limited. The optimum cross-correlation can be computed for each kernel position and thereby drift speeds across the EUV field of view can be derived.

Not all EUV image intensity variations correspond to features in the He<sup>+</sup> distribution. A single image is composed of three subimages from separate cameras (Sandel et al. 2000), each of which can independently protect itself from the Sun and straylight by lowering the detector high voltage and a roll-off in image intensity. The flat-field correction and composition of the separate subimages still may leave some artifacts along the seams between the subimages. Such systematic effects must be guarded against.

A prominent feature of EUV images is noise. Noise can hide the existing plasmaspheric structures, but it also might create artificial structure. Both effects would compromise the drift analysis. Noise strongly influences the correlation coefficient analysis of image pairs. Figure 16 (left panel) is an example of how noise manifests itself in this analysis for the cross-correlation of the consecutive images shown in Fig. 15. The red arrows indicate the derived plasma flow, where the legend defines the arrow length scaling. The yellow regions mark the overlap between individual EUV imaging sensors. The flow pattern looks much more systematic when a noise mitigation technique is applied first (Fig. 16, right panel). A filter is used here that replaces each pixel by the median value in its surrounding  $1 R_E \times$

**Fig. 15** Graphical representation of the cross-correlation procedure for determining drift in EUV images. Each panel shows pseudo-density in the solar magnetic (SM) equatorial plane from EUV images on 10 July 2000 at 05:45 UT and 05:55 UT. Pseudo-density increases logarithmically with gray-scale intensity. The dark center is the location of the Earth. The Sun is to the left. (From Gallagher and Adrian 2007)

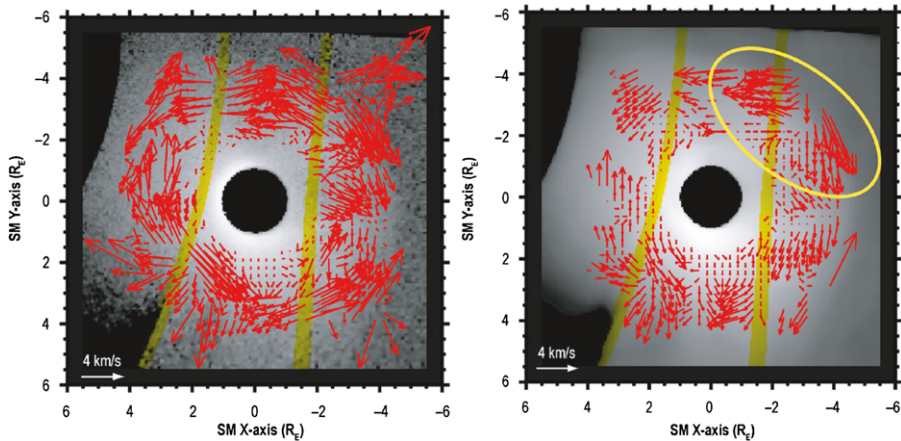
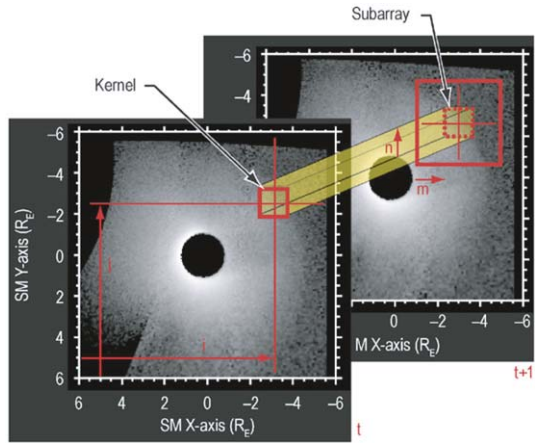


**Fig. 16** Cross-correlation-derived plasmaspheric drift vectors (red arrows). Two sequential 10-minute integrated EUV images are used in the analysis (see Fig. 15). The yellow shading shows where subimages overlap. (Left) Derived from the raw images. (Right) Derived from images in which noise has been reduced by means of a median filter. The yellow oval indicates divergent postmidnight flow. (Adapted from Gallagher and Adrian 2007)

$1 R_E$  spatial box; such a filter preserves edges in images better than linear smoothing filters (see the discussion by Hannequin and Max 2002). An even better treatment of noise is expected from a technique that is based on the properties of Poisson and additive noise, as discussed by Gallagher and Adrian (2007). The challenge is to reduce noise without loss of information.

In the example of Fig. 16, the most pronounced feature is the divergent postmidnight flow (highlighted by the yellow oval) that appears to be real, showing plasmaspheric erosion flows at an early stage. The reliability of the derived drift velocities depends on the errors inherent in the analysis; Gallagher and Adrian (2007) discuss this in some depth and point out that the electric field strengths corresponding to the derived flow velocities are comparable to those derived by an independent technique.

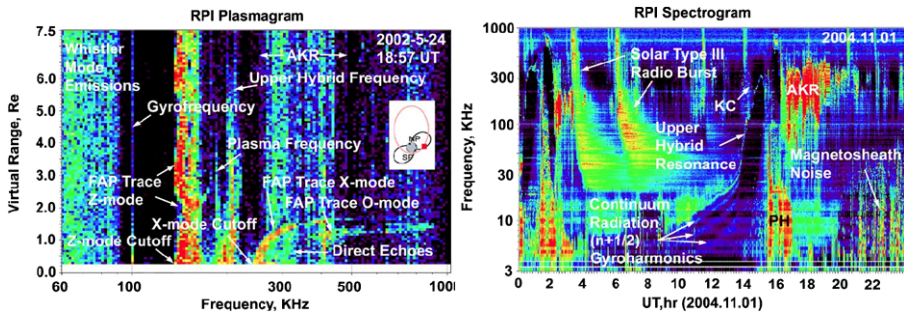


**Fig. 17** Sample IMAGE/RPI active and passive measurements, annotated manually. (Left) A plasmagram showing signal reflections from remote plasma locations (*dark traces*) intermixed with stimulated resonances in the local plasma (*vertical lines*) and natural radio emissions (*vertical bands*). (Right) A typical dynamic spectrogram showing different electromagnetic wave signatures: type III solar radio burst, auroral kilometric radiation (AKR), kilometric continuum (KC), and non-thermal continuum radiation, as well as a number of localized plasma wave signatures: plasmaspheric hiss (PH),  $(n + \frac{1}{2})$  gyroharmonic and upper hybrid resonances, and magnetosheath noise. (Adapted from Galkin et al. 2008)

#### 4.1.3 Outlook

Techniques for EUV image analysis are still fairly recent. Because of noise, straylight, camera artifacts, Earth's shadow, line-of-sight integration, and so on, any analysis will likely necessitate a healthy degree of skepticism and careful scientific judgment, dependent on finding systematic and coherent behavior in time. Results should be checked against in situ observations or models whenever possible.

### 4.2 Interpretation of Remote Sounding and Local Radio Observations

Remote sounding with radio waves has become possible with the IMAGE/RPI instrument's active mode. This unique diagnostic tool allows for a quasi-instantaneous determination of the plasma density at various ranges from the spacecraft. Both sounding from above and from within the plasmasphere are possible. Local radio observations, with IMAGE/RPI's and CLUSTER/WHISPER's passive modes, detect natural radio emissions in the Earth's plasmasphere. WHISPER's active mode has been useful in finding the local plasma properties with more precision. The scientific results obtained from wave observations with RPI and WHISPER in the plasmasphere are reviewed elsewhere in this issue.

While the wave data have a rich scientific content, their interpretation is not easy for space physicists outside the radiowave expert community. To facilitate matters, the radio scientists have developed a number of techniques embedded in a suite of software solutions to enable prospecting, analysis, processing, and content annotation of the data (e.g., Rauch et al. 2006; Galkin et al. 2008). As an example, Fig. 17 shows RPI's science products, the plasmagram (for active sounding) and the spectrogram (for passive observations).

#### 4.2.1 Remote Sounding

The left panel of Fig. 17 shows a typical RPI plasmagram. Received signal strength is plotted as a function of echo delay or virtual range (vertical axis) and operating frequency (horizontal axis) of the radar pulses. Radar echoes from remote plasma structures appear as traces on plasmagrams (dark lines observed above 250 kHz in the left

panel of Fig. 17). Discrete thin traces correspond to field-aligned propagation (FAP) of signals that are guided with little attenuation along a field line (Reinisch et al. 2001; Fung et al. 2003). Plasmagram traces are intermixed with vertical signatures corresponding to the locally excited plasma resonances (e.g., intensification near 200 kHz in the left panel of Fig. 17) and various natural emissions propagating in space.

Field-aligned density profiles are obtained in two steps. First, the traces have to be identified in the plasmagrams, i.e., the frequency–virtual range relation has to be extracted for each trace, a procedure called “scaling the trace”. Fitting of the traces can help to suppress digitization errors. A second step consists of the actual inversion of the traces so as to obtain the density profiles. Both steps have been used extensively in the past for interpreting topside ionosphere sounding data (e.g., Huang and Reinisch 1982). The inversion algorithm solves a set of integral equations that relate the virtual range to the group refractive index along the magnetic field line. The group refractive index is a function of signal frequency, electron plasma frequency, and electron gyrofrequency. The solution of this set of integral equations is a set of electron plasma frequencies along the magnetic field line. Thus a magnetic field-aligned electron density profile is obtained (Huang and Reinisch 1982; Huang et al. 2004). Combination of the local and remote active measurements makes it possible to derive an accurate two-dimensional plasma density distribution in the satellite orbital plane (Huang et al. 2004; Tu et al. 2005; Nsumei et al. 2008), as already discussed in Sect. 3.2 and illustrated in Fig. 14.

Through statistical processing of field-aligned density profiles obtained from plasmagrams, it is possible to construct empirical models of these density distributions (Huang et al. 2004). Such models can serve as the baseline for studies of mass loss and refilling of plasmaspheric flux tubes (Reinisch et al. 2004).

Tu et al. (2005) have used the RPI-derived distribution of electron density  $n_e$  along field lines, as measured by the  $s$  coordinate, in combination with the continuity equation for plasma transport along field lines

$$\frac{\partial n_e}{\partial t} + B \frac{\partial}{\partial s} \left( \frac{n_e V_{\parallel}}{B} \right) = 0$$

to infer the field-aligned electron velocity  $V_{\parallel}$ ; the magnetic field is taken from a model. When there is no significant field-aligned current,  $V_{\parallel}$  also represents the mean ion field-aligned velocity. Assuming a quasi-steady situation and ignoring cross-field transport, they obtain the normalized electron velocity  $V_{\parallel}/V_{\parallel 0} = n_{e0}B/n_eB_0$ , where  $V_{\parallel 0}$ ,  $n_{e0}$ , and  $B_0$  are the values at the wave reflection points below the IMAGE orbit. While this analysis does not provide absolute values for  $V_{\parallel}$ , it clearly shows the upward flow and its acceleration. Different slopes of the density profiles distinguish the plasmasphere from the polar cap. It is even possible to differentiate between the inner plasmasphere where refilling has saturated, and the more outwardly lying plasmasphere where refilling is still ongoing.

Apart from remote sounding, in which the sounder is located outside the plasmasphere, it is also possible to perform sounding from within the plasmasphere. Echoes have been recorded that are the result of ducted propagation in field-aligned plasma density irregularities (Carpenter et al. 2002). The virtual range spreading for such echoes in the plasmagrams is interpreted as being the result of aspect sensitive wave scattering from density irregularities, partial reflection from such irregularities, and propagation in these irregularities. Various characteristics can be derived from the properties of the echoes, such as the transverse size of the irregularities, their extent along the field lines, and the density contrast with their environment. Interpretation of guided echo characteristics is supported by ray-tracing

(Fung and Green 2005). Ray-tracing calculations demonstrate the possible wave propagation paths and establish the conditions for ducted transmission. By performing simulations over the relevant parameter space, insight is gained into the role of duct width, length, and density contrast, and their impact on the appearance of the echoes in a plasmagram.

Detection of stimulated resonances and wave cutoffs in the RPI plasmagrams provides a determination of local plasma density with demonstrated superior accuracy to what conventional density probes can achieve (Reinisch et al. 2001). However, the intricate process of deriving the local plasma density and magnetic field strength values from plasmagram images is known for its high demand of expertise and manual labor. Even greater effort is required to obtain two-dimensional plasma density distributions in the satellite orbital plane using plasmagram traces, as mentioned above. Furthermore, the acquired RPI dataset of 1.2 million plasmagrams incurs a substantial manual expense of data exploration. These considerations warranted development of computer-assisted techniques for data prospecting and interpretation.

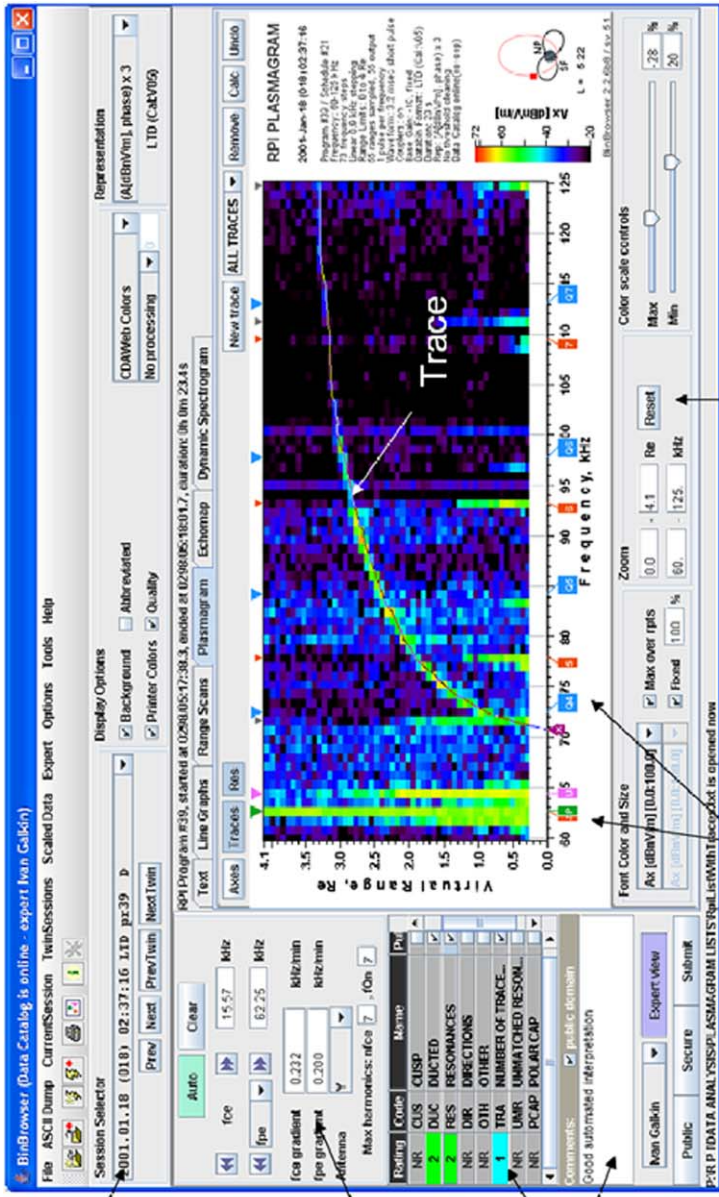
Figure 18 shows a screenshot of the RPI BinBrowser software (Galkin et al. 2008) with the plasmagram for 18 January 2001 at 02:37 UT. A resonance matching algorithm (Galkin et al. 2004a, 2004b), with controls on the left side panel of the BinBrowser graphical user interface, was used to match visible resonance signatures in this plasmagram with their theoretical counterparts, resulting in  $f_{ce} = 15.57$  kHz and  $f_{pe} = 62.25$  kHz, well within 0.5 % of the expert-interpreted values. After the interpretation process is complete, a record of all plasmagram-derived data, together with the expert classification ratings, is added to the RPI Level 2 data repository. This Internet-accessible expert rating service provides a much needed means to tag data by physical content, which makes understanding the plasmagram data an easier exercise to many.

The RPI Level 2 data repository has been used as a testbed for the intelligent data prospecting algorithm CORPRAL (Galkin et al. 2004a, 2004b) that has automatically pre-processed all 1.2 million plasmagrams to search for echo traces. This prospecting algorithm does not provide scientific interpretations of plasmagrams; it merely locates plasmagrams containing echo traces. However, a number of scenarios have emerged that use the number of traces per plasmagram as the database query criterion to restrict data search to relevant data examples. CORPRAL annotations are exploited to find sequences of plasmagrams with traces, corresponding to plasmasphere traversals, for use in calculations of two-dimensional distributions of plasma density in the orbital plane. Also, plasmagrams with a large number of traces can be retrieved to find the most spectacular cases of wave propagation.

#### 4.2.2 Local Plasma Observations

The right panel of Fig. 17 shows a typical RPI dynamic spectrogram, a time history plot of passive measurements of wave intensities as a function of frequency. The RPI detects signatures of various emissions as it orbits the Earth, including intense auroral kilometric radiation (AKR), solar type III radio bursts, plasmaspheric hiss (PH), kilometric continuum (KC), and VLF noise in the magnetosheath. The observed signatures reflect wave generation and propagation mechanisms that are indicative of major physical processes in the Sun–Earth environment.

For illustration, Fig. 19 presents the timeline of RPI passive observations during four days in October 2003, covering the Halloween storm. While these observations do not specifically address plasmaspheric physics, they do illustrate the capabilities of RPI's passive mode in detecting a plethora of waves over a broad frequency range. The dynamic spectrogram shows two Type III solar radio bursts on 28 October at 11:04 UT and on 29 October at 20:46 UT



Data Locator

Automated Resonance Matching Algorithm

Expert Ratings

Labeled resonances

Optimized visualization settings

**Fig. 18** Screenshot of the RPI BinBrowser software tool showing an active measurement (plasmagram) interpreted with the help of a resonance matching algorithm (Galkin et al. 2004a, 2004b). The algorithm detects resonance signatures using image filters and seeks the optimal match between these signatures and a model that accounts for the relation between resonance frequencies and the gradients in the underlying media due to movement of the satellite during the measurement

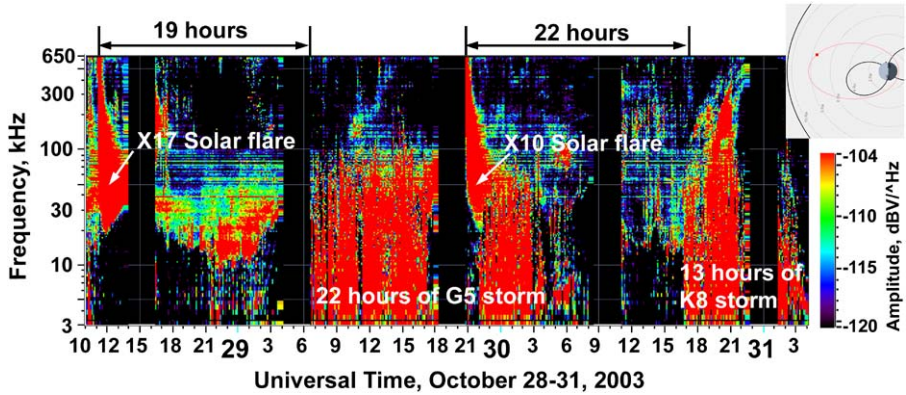


**Fig. 19** IMAGE/RPI passive measurements (spectrogram) showing the timeline of the October 2003 Halloween storm. Two solar events causing Type III solar radio bursts on 28 October 2003 at 11:04 UT and on 29 October 2003 at 20:46 UT are responsible for two geomagnetic storms seen in the spectrogram as intense magnetosheath emissions. The *upper right corner insert* shows the typical IMAGE orbit during the events

correspond to X-category flares. Associated coronal mass ejections were ultimately responsible for two geomagnetic storms seen in the RPI spectrogram as intense magnetosheath emissions generated by turbulent plasma flow across the magnetopause. The ability to monitor such major perturbations are obviously relevant for understanding the magnetospheric context of subsequent plasmasphere observations.

The upper hybrid band and the lower frequency edge of the continuum radiation are nearly always visible in the RPI spectrograms. These spectra can be fitted semi-automatically so as to extract the in situ electron plasma frequency  $f_{pe}$  from the RPI database for the whole mission, from launch in 2000 to end 2005, as well as the electron density  $n_e$ , which can be found from the relation  $f_{pe} [\text{kHz}] \approx 9(n_e [\text{cm}^{-3}])^{1/2}$ . When an upper hybrid band is present, the fitting technique makes use of the fact that the band extends from the greater of  $f_{pe}$  and the electron cyclotron frequency  $f_{ce}$  to the upper-hybrid frequency  $f_{uh}$ , given by  $f_{uh}^2 = f_{pe}^2 + f_{ce}^2$  (Benson et al. 2004). Since IMAGE did not carry a magnetometer, a magnetic-field model is used to obtain  $f_{ce}$  in the fitting technique. If the continuum edge is present, fitting the edge with a hyperbolic tangent function can determine  $f_{pe}$ . Fitting techniques can be automated so as to apply the appropriate method to either the continuum edge or the upper hybrid band. User interaction can help to assess the quality of the fit. Figure 20 shows a spectrogram obtained during a plasmasphere pass on 1 September 2002, which reveals a plasmasphere with the signature of a plume around 13:50–14:30 UT. The black solid triangles denote  $f_{pe}$  calculated from successful fits to the upper hybrid band, while the black solid circles denote  $f_{pe}$  obtained from fitting the lower edge of the continuum band. Open black circles and triangles denote manually corrected points. Their number is limited, illustrating that the automatic procedure is very effective. The red open circles indicate the  $f_{ce}$  values computed from the Tsyganenko T96 magnetic field model (Tsyganenko and Stern 1996). Open magenta symbols denote values that have been discarded by the automatic fitting routine. The figure shows that the model  $f_{ce}$  delimits the upper frequency extent of the low frequency whistler noise band. Also visible are multiple  $n + \frac{1}{2}$  emission bands (Benson et al. 2001) between the continuum edge and the whistler noise band, which occur at approximately  $(n + \frac{1}{2})f_{ce}$  where  $n = 1, 2, \dots$

The CLUSTER/WHISPER wave sounder uses an approach that is slightly different from the IMAGE/RPI, mainly because of its more limited frequency band 2–80 kHz. In its passive

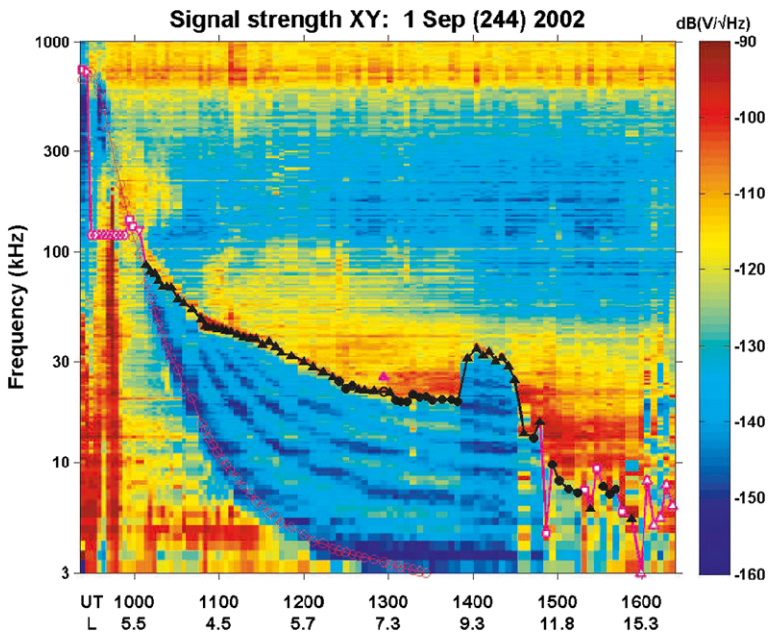


**Fig. 20** IMAGE/RPI passive measurements (spectrogram) for a plasmasphere crossing on 1 September 2002, showing a plasmaspheric plume around 13:50–14:30 UT. *Black solid triangles* denote  $f_{pe}$  values from fitting the upper hybrid band, while *black solid circles* denote  $f_{pe}$  obtained from fitting the lower edge of the continuum band. *Open black circles and triangles* represent manually corrected points. *Open red circles* indicate  $f_{ce}$  values computed from the T96 magnetic field model. *Open magenta symbols* denote discarded points. (Courtesy of Phillip Webb, GSFC)

mode, the receiver monitors natural emissions in that frequency band. Particular wave signatures lead to an independent estimation of  $f_{pe}$  from local wave cut-off properties (Canu et al. 2001). In its active mode, the sounder analyzes the pattern of resonances triggered in the medium locally by a radio pulse. This also allows for the identification of  $f_{pe}$  (Trotignon et al. 2001, 2003). As the plasma resonance signal often is stronger, the precision tends to be higher. Because of WHISPER's frequency limits, this method is useful only in the outer plasmasphere for densities between 0.05 and 80 cm<sup>-3</sup>.

These radio measurements provide only a local characterization of the plasma. Of course, a radial density profile is obtained during a spacecraft pass through the plasmasphere, but that does not provide a global picture, except in a statistical sense (e.g., Goldstein et al. 2003c). To obtain non-local results, in situ data from several spacecraft must be combined. This can be done with CLUSTER by means of general multipoint analysis techniques, such as timing certain events visible in the spectrograms of all spacecraft, or computing gradients of wave data (of  $f_{pe}$  or the derived plasma density, of wave intensities in a particular spectral range, ...). Such general techniques are discussed in Sects. 4.3–4.5. Another way of using local data in a global analysis is to relate the local data to remote sensing data. Examples of this approach are correlated studies between EUV global images and RPI or WHISPER local  $f_{pe}$  observations, for instance, for studying plasmaspheric plume densities (Garcia et al. 2003; Darrouzet et al. 2006a). Both types of observation are complementary: The local measurements give a detailed picture, avoiding line-of-sight integration effects, while the global data provide the context of those measurements.

A specific radio data analysis technique is multiple direction-finding. Direction-finding is an established technique that exploits the fact that the spacecraft are spinning: If the wave is electromagnetic, propagating in the ordinary (O) mode (quasi-circular polarization) and coming from a fixed and limited source, the spin modulation can be used to determine the projection of the direction of propagation onto the antenna spin plane (Gurnett 1975; Gough 1982; Calvert 1985; Kasaba et al. 1998; Reinisch et al. 1999; Décréau et al. 2004). As the antennae on board the CLUSTER satellites rotate in the  $X_{GSE}Y_{GSE}$  plane, the WHISPER instrument measures the  $\mathbf{E}_{xy}$  projection of the wave electric field onto that plane. Considering the general case of elliptic polarization (with circular and linear polarization as particular cases),  $\mathbf{E}_{xy}$  will describe an ellipse whose major axis gives the intensity of the wave electric field. Since the  $\mathbf{k}$ -vector is perpendicular to the wave plane, the wave propagation direction in the spin plane is obtained when the antennae are parallel to the minor axis, i.e., when the lowest value of the electric field is measured. To be useful, it should be easy to differentiate the minor axis from the major axis, so situations where the wave polarization is linear and where the wave plane is perpendicular to the spin plane are preferred. The CLUSTER satellites have a 4 s spin period. As the electric field rotates much quicker, many  $\mathbf{E}_{xy}$  rotation cycles are measured at a given position of the antennae. The measured signal is therefore modulated and can be modelled by

$$E_{\text{antennae}}^2 = E_0^2[1 + \alpha^2 \cos(2\omega t - \phi)]$$

where  $E_0$  is the maximum amplitude measured,  $\phi$  denotes the angle between the antennae and the  $X_{GSE}$  axis,  $\omega$  is the angular velocity of the antennae, and  $\alpha$  is the modulation index factor ( $0 \leq \omega \leq 1$ ). Using a minimum variance method, it is possible to fit the data and to determine  $E_0$ ,  $\alpha$ , and  $\phi$ , i.e., the direction of propagation of the wave projected into the spin plane. The multi-spacecraft aspect of multiple direction finding consists of combining the direction-finding results from several spacecraft observing waves from the same source. Plotting the directions of propagation obtained from two spacecraft in a diagram, two lines are obtained that intersect at the projection of the source position in the spin plane. The source of the wave is then located somewhere in a column parallel to the  $Z_{GSE}$  axis and crossing the point of intersection. In practice, a third and/or fourth satellite are needed to confirm the result. Further, it must be noted that if one finds a modulation index close to 1, the wave has linear polarization and the source is limited in size and remains at a fixed position. For lower modulation factors, the wave is not linearly polarized, or the source might be moving and/or extended in space. Results obtained with this technique on CLUSTER are reported by Grimald et al. (2007). Especially interesting in this context was the tilt manoeuvre operated on one of the spacecraft: With the spin axis of one spacecraft of a closely spaced pair tilted by about  $45^\circ$ , it is possible to test the validity of the hypotheses made in the direction finding method, and sometimes to derive the ellipticity of the observed electric field. In addition, a three-dimensional ray path can be derived.

Another illustration of a multi-instrument (but not really multipoint) technique is the combination of plasmaspheric electron number density profiles from RPI and mass density profiles obtained from ground magnetometer networks through cross-phase determination of the field line resonance frequencies: The result is the computation of an effective “ion mass factor” that measures the admixture of  $H^+$ ,  $He^+$ , and  $O^+$  ions (Dent et al. 2006). Enhanced heavier ion admixtures have been found immediately outside the plasmopause during refilling periods, most likely due to  $O^+$ . Similar work has been done using EUV-derived densities (Grew et al. 2007).

### 4.3 Classical Gradient Computation and the Curlometer

It was already possible in the past to estimate spatial gradients from single-spacecraft data, but only if a number of assumptions were made. For instance, assuming a planar boundary with fixed orientation, one can estimate the gradient with single-point measurements, but the results strongly depend on the orientation of the boundary, which can in principle be obtained by minimum variance analysis (see Sonnerup and Scheible 1998, and references therein), and on the speed of the spacecraft relative to the boundary, which can be estimated from the measured plasma velocity if the interface is a tangential discontinuity. Consequently, it is also possible to estimate the current density. On rather rare occasions, two-spacecraft observations have been used to examine boundary gradients (e.g., Berchem and Russell 1982; Sibeck et al. 2000). The most thorough way of obtaining spatial gradients, without the need for too many assumptions, however, is by making measurements at four non-coplanar points in space as CLUSTER is doing.

#### 4.3.1 Principle

The classical spatial gradient method has been introduced by Harvey (1998). The spatial gradient of a scalar quantity  $f(x, y, z)$  is computed at the centre of the CLUSTER tetrahedron from simultaneous measurements  $f^\alpha$ ,  $\alpha = 1, \dots, 4$  of that quantity. Its components ( $i = x, y, z$ ) are given by

$$\frac{\partial f}{\partial i} = \frac{1}{32} \sum_{j=x,y,z} \left[ \sum_{\alpha=1}^4 \sum_{\beta=1}^4 (f^\alpha - f^\beta) (r_j^\alpha - r_j^\beta) \right] \times \mathbf{R}_{ji}^{-1}, \tag{1}$$

where the  $r^\alpha$  are the spacecraft positions and  $\mathbf{R}$  is the volumetric tensor

$$\mathbf{R}_{ji} = \frac{1}{4} \sum_{\alpha=1}^4 x_j^\alpha x_i^\alpha,$$

which describes the geometrical properties of the tetrahedron. The properties of the spacecraft configuration can be expressed in terms of its eigenvalues and eigenvectors, or in terms of three equivalent geometrical parameters: the characteristic size  $L$ , the elongation  $E$ , and the planarity  $P$ , together with corresponding direction vectors (Robert et al. 1998). The tetrahedron is regular when  $E = P = 0$ . When  $P = 1$ , the satellites are coplanar, whereas when  $E = 1$ , they are colinear. In such cases  $\mathbf{R}$  is singular so that not all gradient components can be computed.

For vector quantities, the gradients can be computed component-wise. For the magnetic field, for instance, the evaluation of the current density vector  $\mathbf{j} = \nabla \times \mathbf{B} / \mu_0$  (at least if time-variability does not play a role) is based on the component gradients. This technique is called the “curlometer” (Chanteur 1998; Chanteur and Harvey 1998; Dunlop and Woodward 1998; Robert et al. 1998; Dunlop et al. 2002; Dunlop and Eastwood 2008). One can also evaluate  $\nabla \cdot \mathbf{B}$  to verify to which extent it is zero; this can give an idea about the precision of the obtained gradients.

#### 4.3.2 Error Determination

Equation (1) yields an average gradient over the spacecraft separation scales, which coincides with the actual gradient only if the gradient is essentially constant over the tetrahedron: The spacecraft have to be embedded in the same structure at the same time. This is

the so-called spatial homogeneity condition. Within the context of the method itself, it is not possible to estimate the error due to the fact that the gradient in reality might not be constant. A priori knowledge about the quantity  $f$  can guide scientific judgment about the realism of the obtained gradients.

A second observation is that (1) involves differences of the measured data values, which can lead to large numerical errors. This is especially true for small spacecraft separation distances, a condition often required to satisfy the homogeneity condition. Gradient computation can therefore only be performed successfully if the measurement errors are small. In particular, the data must be properly cross-calibrated.

The classical gradient computation as defined by (1) is a linear operator acting on the measurements  $f^\alpha$ . The measurement errors will therefore propagate according to the same operator. As the computation involves the inverse of the volumetric tensor  $\mathbf{R}$ , small eigenvalues of this tensor lead to strong error propagation in the corresponding eigenvector direction. Therefore, if the tetrahedron degenerates into a plane or even a line, the errors become excessive. Expressions for the error propagation in terms of  $L$ ,  $P$ , and  $E$  have been given by Darrouzet (2006).

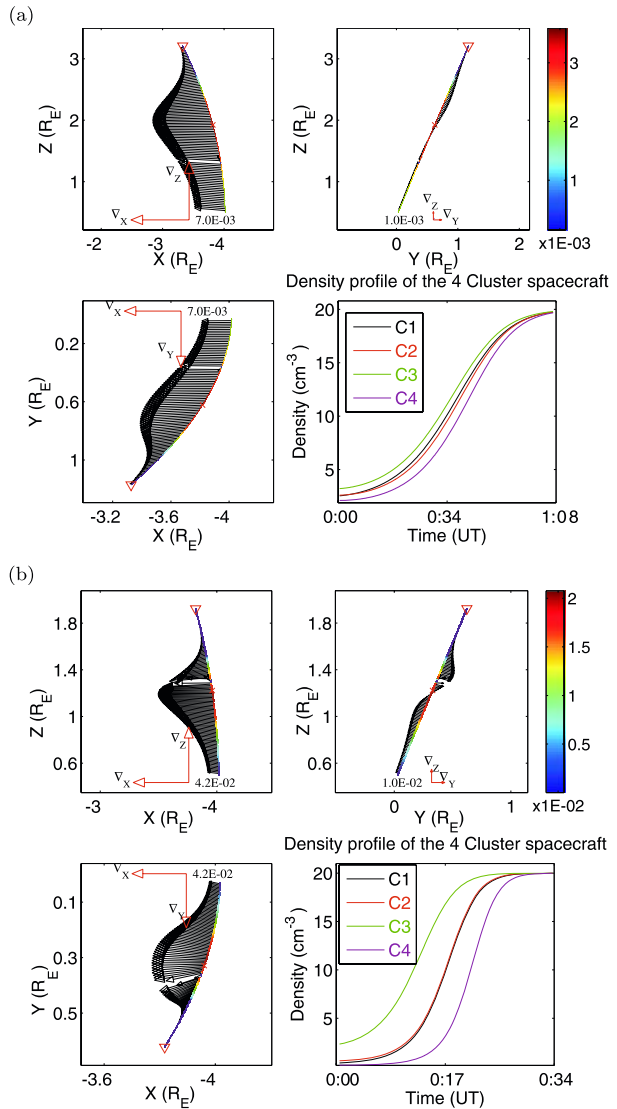
We have already pointed out how sensitive gradient computation is to the errors on the data, since it is based on computing differences. Computing the curl and the divergence of a vector field poses another level of difficulty. As the divergence and each of the components of the curl are sums of terms of the same order of magnitude, but possibly with opposite sign, the relative error on the result can be larger than the relative errors on the individual gradient components, which themselves already carry a significant uncertainty.

The precision of the gradient also depends on the uncertainty on the spacecraft positions. In the context of plasmaspheric studies, which are usually done with medium to large spacecraft separations, this error contribution can be neglected. Similar errors can arise due to imperfect knowledge of the exact time of measurement, owing to uncertainties in spacecraft clock synchronization and instrument cycling or scanning during the data acquisition time (organized in frequency scans in wave instruments, or according to spin for plasma spectrometers); in the plasmasphere such error sources do not matter either.

### 4.3.3 Applications

While the propagation of measurement errors can be evaluated analytically, it is much more difficult to assess the consequences of the homogeneity condition. One can therefore perform some numerical experiments. Figure 21 shows the gradients computed for a simulated crossing by the four CLUSTER spacecraft through an artificial planar density boundary perpendicular to the  $X_{\text{GSE}}$ -axis, given by  $n^\alpha(t) = n_1 + n_2 \tanh(\mathbf{r}_x^\alpha(t)/C)$ , where  $n_1$  and  $n_2$  are given densities and  $C$  the characteristic size of the boundary. In these experiments, real CLUSTER orbits were used (26 February 2001, 00:00–01:30 UT) characterized by a rather regular tetrahedron with  $P < 0.5$  and  $L \approx 0.75$  with a spacecraft separation  $S$  (along  $X_{\text{GSE}}$ ) of  $\sim 1000$  km. Figure 21a corresponds to  $C = 9S$ , a structure larger than the separation distance, while Fig. 21b corresponds to  $C = S$ . Each part of the figure displays the projections of the gradient vectors onto the  $X_{\text{GSE}}Y_{\text{GSE}}$ ,  $Y_{\text{GSE}}Z_{\text{GSE}}$  and  $X_{\text{GSE}}Z_{\text{GSE}}$  planes along the trajectory of the centre of the tetrahedron, as well as the artificial density profiles for the four spacecraft as a function of time. Figure 21a shows that for  $C > S$  the density gradient has both a correct orientation (pointing along  $X_{\text{GSE}}$  only) and magnitude, with an error of around 5%. When  $C = S$ , the spatial gradient has spurious components in the  $Y_{\text{GSE}}$  and  $Z_{\text{GSE}}$  directions, mainly near the edges of the transition. The error attributable to the homogeneity

**Fig. 21** Artificial density gradient computed for the four CLUSTER orbits on 26 February 2001, 00:00–01:30 UT, crossing an artificial density boundary perpendicular to  $X_{GSE}$ . The spacecraft separation was around 1000 km. The panels show the gradients computed along the trajectory of the center of the tetrahedron and projected onto the  $X_{GSE}Y_{GSE}$ ,  $Y_{GSE}Z_{GSE}$ , and  $X_{GSE}Z_{GSE}$  planes, as well as the artificial density profiles at the four spacecraft, for spatial structure (a) on a 9000 km scale, and (b) on a 1000 km scale. The gradient vectors are indicated by black arrows, the color scale encodes the gradient magnitude, and the red cross and triangle indicate the middle and the end of the trajectory. (Adapted from Darrouzet 2006)



condition is now estimated to be around 10%. For even smaller structures ( $C < S$ ), the gradient technique is no longer valid. In conclusion, the homogeneity condition indeed plays a decisive role.

Darrouzet et al. (2006a, 2006b) have applied the classical gradient computation technique to plasmaspheric densities derived from the WHISPER  $f_{pe}$  data. The discrete frequency scale on WHISPER has a half-step of 163 Hz. For densities around  $10 \text{ cm}^{-3}$ , this implies a relative error of  $\sim 1\%$ , or  $0.1 \text{ cm}^{-3}$ . A typical density difference between simultaneous measurements of  $2 \text{ cm}^{-3}$  then leads to a relative precision on the density gradient of typically 5%. In addition, one has to consider the error due to the homogeneity condition, which varies from event to event.

The curlometer based on the classical gradient computation has been applied to CLUSTER magnetic field measurements in the plasmasphere by Vallat et al. (2005), thereby detecting a westward ring current near the equator and field-aligned currents at the plasma sheet boundary.

Gradient techniques, and the curlometer in particular, have been extensively used in the CLUSTER community for studying the magnetopause current layer (e.g., Dunlop and Balogh 2005; De Keyser et al. 2005; Dunlop et al. 2006). These studies, mostly involving the smallest spacecraft separations, lead to results that are consistent with a Chapman-Ferraro current, often showing signatures of magnetospheric surface waves, of reconnection, or of flux transfer events. Current densities have also been computed successfully in the magnetotail current sheet. Other applications include measuring the current density in the heliospheric current sheet (Eastwood et al. 2002).

#### 4.4 Least-Squares Techniques for Gradient Computation

The validity of the classical gradient computation depends on the spatial homogeneity requirement. A recent generalization, least-squares gradient computation, is based on homogeneity in space–time. This improved gradient technique can provide a total error estimate on the result (De Keyser et al. 2007; De Keyser 2008).

##### 4.4.1 Principle

Least-squares gradient computation collects all measurements in a space–time region in which the gradient is essentially constant. Consider a scalar field  $f(\mathbf{x}, t)$  that is sampled  $N$  times, at positions and times  $\mathbf{x}_i = [x_i; y_i; z_i; t_i]$ . The measurements  $f_i$  have known random error variances  $\delta f_{\text{meas},i}^2$ . To illustrate the idea, consider the 2-dimensional situation sketched in Fig. 22. We want to compute the gradient at  $\mathbf{x}_0$  from measurements  $\mathbf{x}_i$  made by several spacecraft. The field  $f$  can be locally approximated by a Taylor expansion around  $\mathbf{x}_0$ . With  $\Delta\mathbf{x} = \mathbf{x} - \mathbf{x}_0$ , and denoting the function value, the gradient, and the hessian at  $\mathbf{x}_0$  by  $f_0$ ,  $\mathbf{g}_0 = \nabla_{\mathbf{x}t} f_0$ , and  $\mathbf{H}_0 = \nabla_{\mathbf{x}t} \nabla_{\mathbf{x}t}^\top f_0$ , this expansion gives

$$f(\mathbf{x}) = f_0 + \Delta\mathbf{x}^\top \mathbf{g}_0 + \frac{1}{2} \Delta\mathbf{x}^\top \mathbf{H}_0 \Delta\mathbf{x} + \dots \quad (2)$$

This expansion can be truncated after the linear term, thus defining the approximating function  $f_{\text{approx}}(\mathbf{x}) = f_0 + \Delta\mathbf{x}^\top \mathbf{g}_0$  and the approximation error  $\delta f_{\text{approx}}(\mathbf{x}) = \frac{1}{2} \Delta\mathbf{x}^\top \mathbf{H}_0 \Delta\mathbf{x} + \dots$ . Requiring that the approximation matches the measurements,

$$f_{\text{approx}}(\mathbf{x}_i) - f_i = 0, \quad (3)$$

results in a system for  $f_0$  and  $\mathbf{g}_0$  with  $N$  equations, one for each measurement. The number of unknowns,  $M$ , is 5. In practical situations in the plasmasphere, this system is overdetermined ( $N \gg M$ ); it can be solved in a least-squares sense.

Approximation (2) is valid in a region around  $\mathbf{x}_0$  that can be described by a 4-dimensional ellipsoid in space–time (dark shaded ellipse in the 2-dimensional analog of Fig. 22); this ellipsoid reflects the homogeneity conditions. It is uniquely specified by a set of four mutually orthogonal unit vectors (the homogeneity directions) and by the associated homogeneity length and time scales. The approximation error  $\delta f_{\text{approx}}$  grows with distance from  $\mathbf{x}_0$ , measured with a norm based on the homogeneity lengths and directions. The total error on each measurement can then be estimated as  $\delta f_i^2 = \delta f_{\text{meas},i}^2 + \delta f_{\text{approx},i}^2$ .

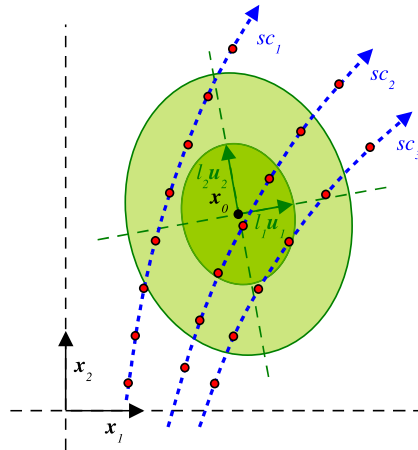


**Fig. 22** The least-squares gradient algorithm uses data from a set of points in space–time, represented here as a 2-dimensional space  $(x_1, x_2)$ . The data are obtained along the trajectories of several spacecraft (red dots on the dotted lines). The homogeneity condition is expressed by associating with each data point an error that grows with distance from  $x_0$ , the point where the gradient is computed. This distance is measured in the frame  $(l_1u_1, l_2u_2)$ . Points inside the inner ellipse correspond to small distances and a small error, points between both ellipses are less relevant, and points outside the outer ellipse are considered irrelevant. (Adapted from De Keyser 2008)

System (3) is treated as a weighted least-squares problem, with the weights being  $1/\delta f_i$ . The system that is actually solved is

$$(f_0 + \Delta \mathbf{x}^\top \mathbf{g}_0 - f_i)/\delta f_i = 0, \tag{4}$$

which is equivalent to minimizing the least-squares problem

$$\chi^2 = \sum_{i=1}^N \frac{(f_0 + \Delta \mathbf{x}^\top \mathbf{g}_0 - f_i)^2}{\delta f_i^2}.$$

We refer to De Keyser et al. (2007) for a description of the solution procedure. The choice of the weights  $1/\delta f_i$  makes sure that measurements with a large total error do not contribute much to the solution. In particular, data acquired well outside the homogeneity domain do not add information.

The gradients of the individual components of a vector field can be obtained by treating each component as a separate scalar field under the simplifying assumption that the approximation errors are not correlated. The number of unknowns at each point is  $M = 3 \times 5 = 15$ . Since the least-squares method can easily handle constraints, magnetic field gradient computations impose the condition  $\nabla \cdot \mathbf{B} = 0$  (so that  $M = 14$ ), thus leading to an improved curlometer.

In situations of strong time-variability the homogeneity time scale is short and one can only use simultaneous measurements. The overdetermined system then is simplified: The time derivatives can be removed from the system, so that  $M = 4$  for the gradient of a scalar field,  $M = 12$  for a vector field, and  $M = 11$  for a divergence-free vector field. If exactly four simultaneous measurements are available and if the four points are well within the spatial homogeneity domain (giving them identical  $\delta f_i$ ), the method effectively reduces to the classical algorithm (as demonstrated in detail by De Keyser et al. 2007).

#### 4.4.2 Error Estimates

The effect of the measurement and approximation errors on the result is described by the singular values of the weighted system (4): Small singular values imply strong error propagation. The singular values offer a convenient generalization of the tetrahedron geometric factors (Robert et al. 1998) and allow one to diagnose when the problem is ill-conditioned. As a result, the least-squares gradient algorithm provides reliable total error estimates on the computed gradient.

#### 4.4.3 Applications

One of the practical benefits of this technique is its robustness. It can handle short data gaps, something that is problematic for the classical gradient algorithm. A particular advantage of the technique is that it may be applied in situations with less than four instruments if constraints are imposed. It can also exploit data from more than four spacecraft. In fact, the actual number of spacecraft does not matter; what is important is the space–time distribution of the measurement points.

While the gradients obtained with the new method typically do not differ much from those obtained with the classical gradient method, one now obtains a quantitative estimate of the total error on the results. The reliability of this estimate depends on the specified homogeneity properties. De Keyser et al. (2007) assume that the homogeneity parameters are all given. While suitable values can be chosen based on physical considerations, this may not be easy to do in practice. It appears possible to introduce heuristic techniques to estimate at least some of the homogeneity properties automatically, so that each gradient can be computed with the optimal set of data points; the error estimates on the gradient then are more realistic (De Keyser 2008).

The homogeneity scales reflect the physical structures to be studied. Whatever the scales, the least-squares method will always produce a result, but whether the computed gradients are accurate depends on the nature of the data and the quality of the space–time sampling. With CLUSTER in the plasmasphere, a good gradient can be obtained when the homogeneity scales are on the order of, or larger than, the spacecraft separations in space and time. Homogeneity lengths of a few hundreds of kilometers and a time scale of 1 minute are usually fine, although finer-scale plasmaspheric structures may be formed more rapidly when geomagnetic activity is stronger, necessitating smaller homogeneity scales. Some CLUSTER applications of the technique are described elsewhere in this issue (Darrouzet et al. 2008; Matsui et al. 2008).

### 4.5 Time-Delay Analysis with Multiple Spacecraft

The limitations of the homogeneity condition can be overcome by making certain assumptions about the objects that are observed. For a magnetospheric interface, for instance, one can perform an analysis of the time delays between the consecutive interface crossings by the four CLUSTER spacecraft in the assumption that the interface is planar.

#### 4.5.1 Method

The basic assumption is that the interface is locally planar, that it moves at a constant speed, that its orientation does not change, and that its characteristic evolution time is longer than the time between the consecutive crossings. The time-delay analysis takes as input the time

delays  $t_\alpha - t_\beta$  between the crossing of the interface for all spacecraft pairs  $(\alpha, \beta)$  as well as the position differences  $\mathbf{r}^\alpha - \mathbf{r}^\beta$ . The method determines the orientation of the interface, as given by its normal direction  $\mathbf{n}$ , and its speed,  $V_n$ , in the normal direction. The method is based on the following set of relations:

$$\frac{1}{V_n} (\mathbf{r}^\alpha - \mathbf{r}^\beta) \cdot \mathbf{n} = t_\alpha - t_\beta$$

for all distinct pairs. For the case of CLUSTER, there are 6 such pairs, of which (at most) 3 are independent. There are also 3 unknowns: 2 independent components of  $\mathbf{n}$  (which is a unit vector) and  $V_n$ . There may be degenerate spatial configurations for which no solution can be found.

#### 4.5.2 Applications

The important advantage of time delay analysis is that it does not require all spacecraft to be within the transition at the same time. This makes the technique peculiarly interesting for intrinsically thin interfaces, such as the bow shock and the magnetopause, for which more evolved versions of the technique have been developed (Haaland et al. 2004). But even for interfaces that are not really thin, this tool can help in situations where the spacecraft separation is simply too large.

Attractive targets for this method in the plasmasphere are density interfaces, such as the plasmopause itself, the edges of a plasmaspheric plume, or density irregularities. The conditions of slow dynamic evolution, planarity, constant orientation, and constant speed are often likely to be satisfied, except perhaps for smaller-scale density irregularities. Darrouzet et al. (2004, 2006a) have applied the technique to plasmaspheric density irregularities and plume interfaces.

## 5 Conclusions and Outlook

The new observational strategies of IMAGE and CLUSTER have already resulted in a number of scientific advances in plasmaspheric research.

The detection of rich detail in IMAGE/EUV global images provides a better understanding of plasmasphere structure. We have reviewed the most frequently used data processing tools, including image inversion and the approximate technique of minimum- $L$  projection and pseudo-density determination. We have highlighted one example of the added value that new tools can bring: By cross-correlating details in subsequent images, the overall plasma convection pattern in the inner magnetosphere can be inferred, from which the convection electric field can be deduced. Such global scale results should be helpful for studying the global and mesoscale electric fields that are responsible for plasmasphere dynamics, including the magnetospheric electric fields responsible for subauroral polarization streams observed in the ionosphere (Goldstein et al. 2003b), and for studying the coupling to the ring current and the ionosphere (Goldstein et al. 2002; Khazanov et al. 2003; Gallagher et al. 2005; Liemohn and Brandt 2005). Interesting in this respect are studies that combine EUV global images with global images from the HENA and MENA neutral atom imagers to investigate the ring current–plasmasphere interaction (Gurgiolo et al. 2005).

The IMAGE/RPI wave instrument provides a picture of its environment by active radio sounding, thereby discovering, for instance, wave ducts of finite extent along the magnetic field lines. With the emitter inside the structures under study, the radio wave echoes can

reveal a lot of detail of the spacecraft environment. The interpretation of the various wave echoes can be ambiguous; a proper understanding of the types of plasma radio waves and their propagation characteristics is indispensable, as techniques for automated identification of traces and resonances rely on the different wave characteristics. Also noteworthy is the use of ray-tracing algorithms in understanding the plasmagram signatures of wave propagation effects. An interesting application has been the measurement of field-aligned total densities that have permitted renewed study of the microphysics of plasmaspheric refilling (Reinisch et al. 2004; Tu et al. 2005). Data mining tools facilitate searching through the plasmagram database. Local radio measurements by IMAGE/RPI and by CLUSTER/WHISPER have both been exploited using automated plasma resonance recognition algorithms to produce reliable ambient plasma density measurements (Rauch et al. 2006; Galkin et al. 2008). Of particular importance are the multi-spacecraft direction-finding techniques for determining the source location of certain waves (Grimald et al. 2007).

The study of the plasmasphere with CLUSTER multi-spacecraft measurements is only starting to gather momentum. An important aspect is the use of the curlometer technique to compute the current density in the plasmasphere (Vallat et al. 2005; De Keyser et al. 2007). Initial results have been reported concerning the density and field gradients in the plasmasphere (Darrouzet et al. 2006b). Studies of the form and evolution of plasmaspheric plumes confirm and extend IMAGE findings, such as plasmaspheric plumes that span more than 6 hours in local time, and the outward motion of plume tips while moving azimuthally at sub-rotation speed (Darrouzet et al. 2006a). The availability of improved gradient computation techniques will certainly help in situations where the spacecraft separations are not small. Especially in combination with empirical models for the field-aligned density distribution, radial and azimuthal gradients could be computed in many more cases than they are now. As the behavior of the CLUSTER instrumentation in space becomes better understood, their intercalibration is improving so that gradients of quantities other than the FGM magnetic field and the WHISPER densities might be computed as well.

Explaining the morphology of plasmaspheric plumes or notches as revealed by these non-local observations (Darrouzet et al. 2008, this issue) challenges current models for the plasmasphere's dynamic evolution. We refer to Pierrard et al. (2008, this issue) for a review of the state-of-the-art in physics-based plasmaspheric models.

Non-local measurements are very well suited for the construction of empirical models (Reinisch et al. 2008, this issue). IMAGE and CLUSTER have contributed to empirical models of the plasma density in the inner magnetosphere and of the electric field that drives the convection. Empirical models of the broad variety of plasma waves that have been recorded by both missions are being constructed for assessing the effect of wave-particle interactions on the time-evolution of the radiation belts.

As in the past, combining data from various spacecraft and/or on the ground, as well as model simulations, help scientists to arrive at a more global picture of the state of the plasmasphere. Interesting conjunctions between individual spacecraft have been rather rare. The pictures offered by IMAGE/EUV, however, provide the global context for in situ measurements without requiring a conjunction. In particular, combined data analysis with CLUSTER and IMAGE data has turned out to be rewarding (e.g., Darrouzet et al. 2006a).

The acquisition of non-local data, by remote sensing from a single spacecraft as with IMAGE or by combining in situ data from spacecraft constellations as with CLUSTER, has revolutionized space plasma physics. Current and future magnetospheric missions will heavily use these techniques: China's CHANG'E and KUAFU-B spacecraft will use extreme ultraviolet imagers similar to those on IMAGE, and the CROSS-SCALE and WARP missions proposed in the frame of ESA's Cosmic Vision program, as well as NASA's THEMIS and MMS missions, use a multi-spacecraft configuration.

Future plasmasphere missions would have to carry a sufficiently broad suite of experiments that is able to measure the plasma environment, from the cold plasmaspheric populations over the warm ring current plasma to the energetic radiation belt particles. Such missions should study the interactions between all these plasma populations and the fields to further elucidate the dynamical response of the inner magnetosphere at times of disturbed geomagnetic activity. Electron content data routinely inferred from the propagation of radio signals between spacecraft or between spacecraft and the ground undoubtedly will play an important role as well. Practical benefits of such research would include improved predictability of the state of the ionosphere and of the reliability of GPS-based applications, and a more thorough understanding of radiation belt ionization hazards to spacecraft and human crew.

**Acknowledgements** J. De Keyser and F. Darrouzet acknowledge the support by the Belgian Federal Science Policy Office (BELSPO) through the ESA/PRODEX CLUSTER project (contract 13127/98/NL/VJ (IC)). This paper is an outcome of the workshop "The Earth's plasmasphere: A CLUSTER, IMAGE, and modeling perspective" organized by the Belgian Institute for Space Aeronomy in Brussels in September 2007.

## References

- B. Abel, R.M. Thorne, Electron scattering loss in Earth's inner magnetosphere. 1. Dominant physical processes. *J. Geophys. Res.* **103**(A2), 2385–2396 (1994)
- M.L. Adrian, D.L. Gallagher, L.A. Avanov, IMAGE EUV observation of radially bifurcated plasmaspheric features: First observations of a possible standing ULF waveform in the inner magnetosphere. *J. Geophys. Res.* **109**, A01203 (2004)
- V.V. Afonin, K.V. Grechnev, V.A. Ershova, O.Z. Rosté, N.F. Smirnova, Y.A. Schul'chishin, Y. Smilauer, Ion composition and temperature of the ionosphere obtained from the Intercosmos 24 satellite ("Aktivnyi" project) at the maximum of the 22nd solar activity cycle. *Cosmic Res.* **32**(2), 189–198 (1994)
- V.V. Afonin, V.S. Bassolo, J. Smilauer, J.F. Lemaire, Motion and erosion of the nightside plasmopause region and of the associated subauroral electron temperature enhancement: Cosmos-900 observations. *J. Geophys. Res.* **102**(A2), 2093–2103 (1997)
- P.C. Anderson, D.L. Carpenter, K. Tsuruda, T. Mukai, F.J. Rich, Multisatellite observations of rapid subauroral ion drifts (SAID). *J. Geophys. Res.* **106**(A12), 29585–29599 (2001)
- R.R. Anderson, CRRES plasma wave observations during quiet times, during geomagnetic disturbances, and during chemical releases, in *Dusty and Dirty Plasmas, Noise, and Chaos in Space and in the Laboratory*, ed. by H. Kikuchi (Plenum Press, New York, 1994), pp. 73–96
- A. Balogh, C.M. Carr, M.H. Acuña, M.W. Dunlop, T.J. Beek, P. Brown, K.-H. Fornaçon, E. Georgescu, K.-H. Glassmeier, J. Harris, G. Musmann, T. Oddy, K. Schwingenschuh, The Cluster magnetic field investigation: Overview of in-flight performance and initial results. *Ann. Geophys.* **19**(10), 1207–1217 (2001)
- R.F. Benson, V.A. Oshervovich, J. Fainberg, A.F. Vinas, D.R. Ruppert, An interpretation of banded magnetospheric radio emissions. *J. Geophys. Res.* **106**(A7), 13179–13190 (2001)
- R.F. Benson, P.A. Webb, J.L. Green, L. Garcia, B.W. Reinisch, Magnetospheric electron densities inferred from upper-hybrid band emissions. *Geophys. Res. Lett.* **31**, L20803 (2004)
- R.F. Benson, P.A. Webb, J.L. Green, D.L. Carpenter, V.S. Sonwalkar, H.G. James, B.W. Reinisch, Active wave experiments in space plasmas: The Z mode, in *Geospace Electromagnetic Waves and Radiation*, ed. by J.W. Labelle, R.A. Treumann. Lecture Notes in Physics (Springer, Berlin, 2006), pp. 3–35
- J. Berchem, C.T. Russell, The thickness of the magnetopause current layer - ISEE 1 and 2 observations. *J. Geophys. Res.* **87**(A4), 2108–2114 (1982)
- V.V. Bezrukhikh, Results of the measurements of the concentration of charged particles in the plasma cloud of the Earth carried out on board of Elektron 2 and Elektron 4. *Kosm. Issled.* **8**, 273–277 (1970)
- V.V. Bezrukhikh, K.I. Gringauz, The hot zone in the outer plasmasphere of the Earth. *J. Atmos. Terr. Phys.* **38**, 1085–1091 (1976)
- J. Bortnik, U.S. Inan, T.F. Bell, Frequency-time spectra of magnetospherically reflecting whistlers in the plasmasphere. *J. Geophys. Res.* **108**(A1), 1030 (2003)
- P.C. Brandt, D.G. Mitchell, Y. Ebihara, B.R. Sandel, E.C. Roelof, J.L. Burch, R. Demajistre, Global IMAGE/HENA observations of the ring current: Examples of rapid response to IMF and ring current-plasmasphere interaction. *J. Geophys. Res.* **107**(A11), 1359 (2002)

- N.M. Brice, Bulk motion of the magnetosphere. *J. Geophys. Res.* **72**(21), 5193–5211 (1967)
- N.M. Brice, R.L. Smith, Lower hybrid resonance emissions. *J. Geophys. Res.* **70**(1), 71–80 (1965)
- J.L. Burch, IMAGE mission overview. *Space Sci. Rev.* **91**(1–2), 1–14 (2000)
- J.L. Burch, J. Goldstein, B.R. Sandel, Cause of plasmasphere corotation lag. *Geophys. Res. Lett.* **31**(5), L05802 (2004)
- W.C. Burgess, U.S. Inan, The role of ducted whistlers in the precipitation loss and equilibrium flux of radiation belt electrons. *J. Geophys. Res.* **98**(A9), 15643–15665 (1993)
- W.I. Burke, N.C. Maynard, M.P. Hagan, R.A. Wolf, G.R. Wilson, L.C. Gentile, M.S. Gussenhoven, C.Y. Huang, T.W. Garner, F.J. Rich, Electrodynamics of the inner magnetosphere observed in the dusk sector by CRRES and DMSP during the magnetic storm of June 4–6, 1991. *J. Geophys. Res.* **103**(A12), 29399–29418 (1998)
- W. Calvert, DE-1 measurements of AKR wave directions. *Geophys. Res. Lett.* **12**(6), 381–384 (1985)
- P. Canu, P.M.E. Décréau, J.G. Trotignon, J.L. Rauch, H.C. Séran, P. Ferreau, M. Lévêque, P. Martin, F.X. Sené, E. Le Guirriec, H. Alleyne, K. Yearby, Identification of natural plasma emissions observed close to the plasmapause by the Cluster-Whisper relaxation sounder. *Ann. Geophys.* **19**(10), 1697–1709 (2001)
- D.L. Carpenter, Whistler evidence of a “knee” in the magnetospheric ionization density profile. *J. Geophys. Res.* **68**(6), 1675–1682 (1963)
- D.L. Carpenter, Whistler measurements of the equatorial profile of magnetospheric electron density, in *Progress in Radio Science 1960–1996, III, The Ionosphere*, ed. by G.M. Brown (Elsevier, Amsterdam, 1965), pp. 76–91
- D.L. Carpenter, Whistler studies of the plasmapause in the magnetosphere, I. Temporal variations in the position of the knee and some evidence on plasma motions near the knee. *J. Geophys. Res.* **71**(3), 693–709 (1966)
- D.L. Carpenter, Relations between the dawn minimum in the equatorial radius of the plasmapause and  $Dst$ ,  $K_p$ , and local  $K$  at Byrd Station. *J. Geophys. Res.* **72**(11), 2969–2971 (1967)
- D.L. Carpenter, Remarks on the ground-based whistler method of studying the magnetospheric thermal plasma. *Ann. Geophys.* **26**(2), 363–370 (1970a)
- D.L. Carpenter, Whistler evidence of the dynamic behavior of the duskside bulge in the plasmasphere. *J. Geophys. Res.* **75**(19), 3837–3847 (1970b)
- D.L. Carpenter, OGO 2 and 4 VLF observations of the asymmetric plasmapause near the time of SAR arc events. *J. Geophys. Res.* **76**(16), 3644–3650 (1971)
- D.L. Carpenter, Remote sensing the Earth’s plasmasphere. *Rad. Sci. Bull.* **308**, 13–29 (2004)
- D.L. Carpenter, R.R. Anderson, An ISEE/Whistler model of equatorial electron density in the magnetosphere. *J. Geophys. Res.* **97**(A2), 1097–1108 (1992)
- D.L. Carpenter, B.L. Giles, C.R. Chappell, P.M.E. Décréau, R.R. Anderson, A.M. Persoon, A.J. Smith, Y. Corcuff, P. Canu, Plasmasphere dynamics in the duskside bulge region: A new look at an old topic. *J. Geophys. Res.* **98**(A11), 19243–19271 (1993)
- D.L. Carpenter, J. Lemaire, The plasmasphere boundary layer. *Ann. Geophys.* **22**(12), 4291–4298 (2004)
- D.L. Carpenter, R. Walter, R.E. Barrington, D.J. McEwen, Alouette 1 and 2 observations of abrupt changes in whistler rate and of VLF noise variations at the plasmapause—A satellite-ground study. *J. Geophys. Res.* **73**(9), 2929–2940 (1968)
- D.L. Carpenter, A.J. Smith, B.L. Giles, C.R. Chappell, P.M.E. Décréau, A case study of plasma structure in the dusk sector associated with enhanced magnetospheric convection. *J. Geophys. Res.* **97**(A2), 1157–1166 (1992)
- D.L. Carpenter, M.A. Spasojević, T.F. Bell, U.S. Inan, B.W. Reinisch, I.A. Galkin, R.F. Benson, J.L. Green, S.F. Fung, S.A. Boardsen, Small-scale field-aligned plasmaspheric density structures inferred from the radio plasma imager on IMAGE. *J. Geophys. Res.* **107**(A9), 1258 (2002)
- G. Chanteur, Spatial interpolation for four spacecraft: Theory, in *Analysis Methods for Multi-Spacecraft Data*, ed. by G. Paschmann, P.W. Daly. ISSI SR-001 (ESA Publications Division, 1998), pp. 349–369
- G. Chanteur, C.C. Harvey, Spatial interpolation for four spacecraft: Application to magnetic gradients, in *Analysis Methods for Multi-Spacecraft Data*, ed. by G. Paschmann, P.W. Daly (ESA Publications Division, 1998), pp. 371–393, ISSI SR-001
- C.R. Chappell, K.K. Harris, G.W. Sharp, A study of the influence of magnetic activity on the location of the plasmapause as measured by OGO 5. *J. Geophys. Res.* **75**(1), 50–56 (1970)
- R.H. Comfort, Plasmasphere thermal structure as measured by ISEE-1 and DE-1. *Adv. Space Res.* **6**(3), 31–40 (1986)
- P.D. Craven, D.L. Gallagher, R.H. Comfort, Relative concentration of  $\text{He}^+$  in the inner magnetosphere as observed by the DE 1 retarding ion mass spectrometer. *J. Geophys. Res.* **102**(A2), 2279–2289 (1997)
- F. Darrouzet, Etude de la magnétosphère terrestre par l’analyse multipoint des données de la mission CLUSTER. Contributions à la caractérisation des frontières et de la magnétosphère interne, Ph.D. thesis, University of Orléans, France (2006). [http://www.aeronomie.be/plasmasphere/pdf/Darrouzet\\_PhDThesis\\_UniversityOrleans\\_20060607.pdf](http://www.aeronomie.be/plasmasphere/pdf/Darrouzet_PhDThesis_UniversityOrleans_20060607.pdf)

- F. Darrouzet, P.M.E. Décréau, J. De Keyser, A. Masson, D.L. Gallagher, O. Santolík, B.R. Sandel, J.G. Trotignon, J.L. Rauch, E. Le Guirriec, P. Canu, F. Sedgemore, M. André, J.F. Lemaire, Density structures inside the plasmasphere: Cluster observations. *Ann. Geophys.* **22**(7), 2577–2585 (2004)
- F. Darrouzet, J. De Keyser, P.M.E. Décréau, D.L. Gallagher, V. Pierrard, J.F. Lemaire, B.R. Sandel, I. Dandouras, H. Matsui, M. Dunlop, J. Cabrera, A. Masson, P. Canu, J.G. Trotignon, J.L. Rauch, M. André, Analysis of plasmaspheric plumes: CLUSTER and IMAGE observations. *Ann. Geophys.* **24**(6), 1737–1758 (2006a)
- F. Darrouzet, J. De Keyser, P.M.E. Décréau, J.F. Lemaire, M.W. Dunlop, Spatial gradients in the plasmasphere from Cluster. *Geophys. Res. Lett.* **33**(8), L08105 (2006b)
- F. Darrouzet, D.L. Gallagher, N. André, D.L. Carpenter, I. Dandouras, P.M.E. Décréau, J. De Keyser, R.E. Denton, J.C. Foster, J. Goldstein, M.B. Moldwin, B.W. Reinisch, B.R. Sandel, J. Tu, Plasmaspheric density structures and dynamics: Properties observed by the CLUSTER and IMAGE missions. *Space Sci. Rev.* (2008, this issue)
- J. De Keyser, Least-squares multi-spacecraft gradient calculation with automatic error estimation. *Ann. Geophys.* **26**(11), 3295–3316 (2008)
- J. De Keyser, F. Darrouzet, M.W. Dunlop, P.M.E. Décréau, Least-squares gradient calculation from multipoint observations of scalar and vector fields: Methodology and applications with Cluster in the plasmasphere. *Ann. Geophys.* **25**(4), 971–987 (2007)
- J. De Keyser, M.W. Dunlop, C.J. Owen, B.U.O. Sonnerup, S.E. Haaland, A. Vaivads, G. Paschmann, R. Lundin, L. Rezeau, Magnetopause and boundary layer. *Space Sci. Rev.* **118**(1–4), 231–320 (2005)
- P.M.E. Décréau, C. Beghin, M. Parrot, Global characteristics of the cold plasma in the equatorial plasmapause region as deduced from the GEOS 1 mutual impedance probe. *J. Geophys. Res.* **87**(A2), 695–712 (1982)
- P.M.E. Décréau, C. Ducoin, G. Le Rouzic, O. Randriamboarison, J.L. Rauch, J.G. Trotignon, X. Vallières, P. Canu, F. Darrouzet, M.P. Gough, A. Buckley, T.D. Carozzi, Observation of continuum radiations from the CLUSTER fleet: First results from direction finding. *Ann. Geophys.* **22**(7), 2607–2624 (2004)
- P.M.E. Décréau, P. Ferreau, V. Krasnosels'kikh, E. Le Guirriec, M. Lévêque, P. Martin, O. Randriamboarison, J.L. Rauch, F.X. Sené, H.C. Séran, J.G. Trotignon, P. Canu, N. Cornilleau, H. de Féraudy, H. Alleyne, K. Yearby, P.B. Mørgensen, G. Gustafsson, M. André, D.A. Gurnett, F. Darrouzet, J. Lemaire, C.C. Harvey, P. Travnicek, Early results from the Whisper instrument on Cluster: An overview. *Ann. Geophys.* **19**(10), 1241–1258 (2001)
- Z.C. Dent, I.R. Mann, J. Goldstein, F.W. Menk, L.G. Ozeke, Plasmaspheric depletion, refilling, and plasmapause dynamics: A coordinated ground-based and IMAGE satellite study. *J. Geophys. Res.* **111**, A03205 (2006)
- R.E. Denton, J. Goldstein, J.D. Menietti, Field line dependence of magnetospheric electron density. *Geophys. Res. Lett.* **29**(24), 2205 (2002)
- J.W. Dungey, The theory of the quiet magnetosphere, in *Proceedings of the 1966 Symposium on Solar-Terrestrial Physics*, ed. by J.W. King, W.S. Newman (Belgrade, 1967), pp. 91–106
- M.W. Dunlop, A. Balogh, Magnetopause current as seen by Cluster. *Ann. Geophys.* **23**(3), 901–907 (2005)
- M.W. Dunlop, A. Balogh, H.C. Glassmeier, Four-point Cluster application of magnetic field analysis tools: The discontinuity analyzer. *J. Geophys. Res.* **107**(A11), 1385 (2002)
- M.W. Dunlop, J.P. Eastwood, The curlometer and other gradient based methods, in *Multi-Spacecraft Analysis Methods Revisited*, ed. by G. Paschmann, P.W. Daly. ISSI SR-008 (ESA Communications, 2008), pp. 17–25
- M.W. Dunlop, T.I. Woodward, Multi-spacecraft discontinuity analysis: Orientation and motion, in *Analysis Methods for Multi-Spacecraft Data*, ed. by G. Paschmann, P.W. Daly. ISSI SR-001 (ESA Publications Division, 1998), pp. 271–306
- M.W. Dunlop, A. Balogh, Q.-Q. Shi, Z. Pu, C. Vallat, P. Robert, S. Haaland, C. Shen, J.A. Davies, K.-H. Glassmeier, P. Cargill, F. Darrouzet, A. Roux, The curlometer and other gradient measurements with Cluster. *Proceedings of the Cluster and Double Star Symposium, 5th Anniversary of Cluster in Space, ESA SP-598* (2006)
- J.P. Eastwood, A. Balogh, M.W. Dunlop, C.W. Smith, Cluster observations of the heliospheric current sheet and an associated magnetic flux rope and comparisons with ACE. *J. Geophys. Res.* **107**(A11), 1365 (2002)
- C.P. Escoubet, C.T. Russell, R. Schmidt (eds.), *The Cluster and Phoenix Missions* (Kluwer, Dordrecht, 1997)
- J.C. Foster, P.J. Erickson, A.J. Coster, J. Goldstein, F.J. Rich, Ionospheric signatures of plasmaspheric tails. *Geophys. Res. Lett.* **29**(13), 1623 (2002)
- J.C. Foster, W. Rideout, B. Sandel, W.T. Forrester, F.J. Rich, On the relationship of SAPS to storm-enhanced density. *J. Atmos. Sol.-Terr. Phys.* **69**(3), 303–313 (2007)
- S.F. Fung, R.F. Benson, D.L. Carpenter, J.L. Green, V. Jayanti, I.A. Galkin, B.W. Reinisch, Guided echoes in the magnetosphere: Observations by radio plasma imager on IMAGE. *Geophys. Res. Lett.* **30**(11), 1589 (2003)

- S.F. Fung, J.L. Green, Modeling of field-aligned guided echoes in the plasmasphere. *J. Geophys. Res.* **110**(A1), A01210 (2005)
- I. Galkin, B.W. Reinisch, G. Grinstein, G. Khmyrov, A. Kozlov, X. Huang, S. Fung, Automated exploration of the radio plasma imager data. *J. Geophys. Res.* **109**, A12210 (2004a)
- I. Galkin, B.W. Reinisch, X. Huang, R.F. Benson, S. Fung, Automated diagnostics for resonance signature recognition on IMAGE/RPI plasmagrams. *Radio Sci.* **39**(1), RS1015 (2004b)
- I.A. Galkin, G. Khmyrov, A. Kozlov, B.W. Reinisch, Intelligent resident archive for RPI Level 2 data, in *Radio Sounding and Plasma Physics*, ed. by P. Song, J. Foster, M. Mendillo, D. Bilitza. AIP Conf. Proc., vol. 974 (2008), pp. 111–117
- D.L. Gallagher, M.L. Adrian, Two-dimensional drift velocities from the IMAGE EUV plasmaspheric imager. *J. Atmos. Sol.-Terr. Phys.* **69**(3), 341–350 (2007)
- D.L. Gallagher, M.L. Adrian, M.W. Liemohn, Origin and evolution of deep plasmaspheric notches. *J. Geophys. Res.* **110**, A09201 (2005)
- D.A. Galvan, M.B. Moldwin, B.R. Sandel, Diurnal variation in plasmaspheric He<sup>+</sup> inferred from extreme ultraviolet images. *J. Geophys. Res.* **113**, A09216 (2008)
- G. Ganguli, M.A. Reynolds, M.W. Liemohn, The plasmasphere and advances in plasmaspheric research. *J. Atmos. Sol.-Terr. Phys.* **62**(17–18), 1647–1657 (2000)
- L.N. Garcia, S.F. Fung, J.L. Green, S.A. Boardsen, B.R. Sandel, B.W. Reinisch, Observations of the latitudinal structure of plasmaspheric convection plumes by IMAGE-RPI and EUV. *J. Geophys. Res.* **108**(A8), 1321 (2003)
- J. Geiss, H. Balsiger, P. Eberhardt, H.P. Walker, L. Weber, D.T. Young, H. Rosenbauer, Dynamics of magnetospheric ion composition as observed by the GEOS mass spectrometer. *Space Sci. Rev.* **22**(5), 537–566 (1978)
- A.R. Gibby, U.S. Inan, T.F. Bell, Saturation effects in the VLF triggered emission process. *J. Geophys. Res.* **113**, A11215 (2008)
- J. Goldstein, R.W. Spiro, P.H. Reiff, R.A. Wolf, B.R. Sandel, J.W. Freeman, R.L. Lambour, IMF-driven overshielding electric field and the origin of the plasmaspheric shoulder of May 24, 2000. *Geophys. Res. Lett.* **29**(16), 1819 (2002)
- J. Goldstein, B.R. Sandel, W.T. Forrester, P.H. Reiff, IMF-driven plasmasphere erosion of 10 July 2000. *Geophys. Res. Lett.* **30**(3), 1146 (2003a)
- J. Goldstein, B.R. Sandel, M.R. Hairston, P.H. Reiff, Control of plasmaspheric dynamics by both convection and sub-auroral polarization stream. *Geophys. Res. Lett.* **30**(24), 2243 (2003b)
- J. Goldstein, M. Spasojević, P.H. Reiff, B.R. Sandel, W.T. Forrester, D.L. Gallagher, B.W. Reinisch, Identifying the plasmopause in IMAGE EUV data using IMAGE RPI in situ steep density gradients. *J. Geophys. Res.* **108**(A4), 1147 (2003c)
- J. Goldstein, B.R. Sandel, M.F. Thomsen, M. Spasojević, P.H. Reiff, Simultaneous remote sensing and in situ observations of plasmaspheric drainage plumes. *J. Geophys. Res.* **109**, A03202 (2004)
- J. Goldstein, J.L. Burch, B.R. Sandel, Magnetospheric model of subauroral polarization stream. *J. Geophys. Res.* **110**, A09222 (2005)
- J. Goldstein, B.R. Sandel, H.U. Frey, S.B. Mende, Multiple plasmopause undulations observed by the IMAGE satellite on 20 March 2001. *J. Atmos. Sol.-Terr. Phys.* **69**(3), 322–333 (2007)
- M.P. Gough, Non-thermal continuum emissions associated with electron injections: Remote plasmopause sounding. *Planet. Space Sci.* **30**(7), 657–668 (1982)
- J.L. Green, B.W. Reinisch, An overview of results from RPI on Image. *Space Sci. Rev.* **109**(1–4), 183–210 (2003)
- R.S. Grew, F.W. Menk, M.A. Clilverd, B.R. Sandel, Mass and electron densities in the inner magnetosphere during a prolonged disturbed interval. *Geophys. Res. Lett.* **34**, L02108 (2007)
- S. Grimald, P.M.E. Décréau, P. Canu, X. Suraud, X. Vallières, F. Darrouzet, C.C. Harvey, A quantitative test of Jones NTC beaming theory using Cluster constellation. *Ann. Geophys.* **25**(3), 823–831 (2007)
- K.I. Gringauz, The structure of the ionized gas envelope of the Earth from direct measurements in the USSR of local charged particle concentrations. *Planet. Space Sci.* **11**(3), 281–296 (1963)
- K.I. Gringauz, V.V. Bezrukikh, Plasmasphere of the Earth (Review). *Geomagn. Aeron.* **17**(5), 523–533 (1977)
- K.I. Gringauz, V.G. Kurt, V.I. Moroz, I.S. Shklovsky, Results of observations of charged particles observed out to R = 100,000 km with the aid of charged-particle traps on Soviet space rockets. *Astronomicheskii Zhurnal* **37**, 716–735 (1960)
- K.I. Gringauz, V.V. Bezrukikh, V.D. Ozerov, R.E. Rybchinskii, The study of interplanetary ionized gas, high-energy electrons and corpuscular radiation of the Sun, employing three-electrode charged particle traps on the second Soviet space rocket. *Planet. Space Sci.* **9**(3), 103–107 (1962)
- C. Gurgiolo, B.R. Sandel, J.D. Perez, D.G. Mitchell, C.J. Pollock, B.A. Larsen, Overlap of the plasmasphere and ring current: Relation to subauroral ionospheric heating. *J. Geophys. Res.* **110**, A12217 (2005)

- D.A. Gurnett, The Earth as a radio source: The nonthermal continuum. *J. Geophys. Res.* **80**(19), 2751–2763 (1975)
- D.A. Gurnett, U.S. Inan, Plasma wave observations with the Dynamics Explorer 1 spacecraft. *Rev. Geophys.* **26**(2), 285–316 (1988)
- D.A. Gurnett, F.L. Scarf, Summary report on session on new developments, in *Progress in Radio Science, 1963–1966* (International Union of Radio Science, Brussels, 1967), pp. 1106–1107
- G. Gustafsson, M. André, T. Carozzi, A.I. Eriksson, C.-G. Fälthammar, R. Grard, G. Holmgren, J.A. Holtet, N. Ivchenko, T. Karlsson, Y. Khotyaintsev, S. Klimov, H. Laakso, P.-A. Lindqvist, B. Lybekk, G. Marklund, F. Mozer, K. Mursula, A. Pedersen, B. Popielawska, S. Savin, K. Stasiewicz, P. Tanskanen, A. Vaivads, J.E. Wahlund, First results of electric field and density observations by Cluster EFW based on initial months of observations. *Ann. Geophys.* **19**(10–12), 1219–1240 (2001)
- S. Haaland, B.U.Ö. Sonnerup, M.W. Dunlop, A. Balogh, H. Hasegawa, B. Klecker, G. Paschmann, B. Lavraud, H. Rème, Four-spacecraft determination of magnetopause orientation, motion and thickness: Comparison with results from single-spacecraft methods. *Ann. Geophys.* **22**(4), 1347–1365 (2004)
- P. Hannequin, J. Max, Statistical and heuristic image noise extraction (SHINE): A new method for processing Poisson noise in scintigraphic images. *Phys. Medicine Biol.* **47**, 4329–4344 (2002)
- W.B. Hanson, I.B. Ortenburger, The coupling between the protonosphere and the normal F region. *J. Geophys. Res.* **66**(5), 1425–1435 (1961)
- C.C. Harvey, Spatial gradients and the volumetric tensor, in *Analysis Methods for Multi-Spacecraft Data*, ed. by G. Paschmann, P.W. Daly. ISSI SR-001 (ESA Publications Division, 1998), pp. 307–322
- K. Hashimoto, J.J. Green, R.R. Anderson, H. Matsumoto, Review of kilometric continuum, in *Geospace Electromagnetic Waves and Radiation*, ed. by J.W. LaBelle, R.A. Treumann. Lecture Notes in Physics, vol. 687 (Springer, Berlin, 2006), pp. 37–51
- M. Hayakawa, Whistlers, in *Handbook of atmospheric electrodynamics*, ed. by H. Volland, vol. II (CRC, Boca Raton, 1995), pp. 155–194
- M. Hayakawa, S.S. Sazhin, Mid-latitude and plasmaspheric hiss: A review. *Planet. Space Sci.* **40**(10), 1325–1338 (1992)
- S. Heise, N. Jakowski, D. Cooke, Ionosphere/plasmasphere imaging based on GPS navigation measurements from CHAMP and SAC-C, in *Earth Observation with CHAMP: Results from Three Years in Orbit*, ed. by C. Reigber, H. Lühr, P. Schwintzer, J. Wickert (Springer, Berlin, 2005), pp. 471–476
- R.A. Helliwell, VLF wave stimulation experiments in the magnetosphere from Siple Station, Antarctica. *Rev. Geophys.* **26**(3), 551–578 (1988)
- R.A. Helliwell, J.P. Katsufakis, VLF wave injection into the magnetosphere from Siple Station, Antarctica. *J. Geophys. Res.* **79**(16), 2511–2518 (1974)
- R.L. Heyborne, R.L. Smith, R.A. Helliwell, Latitudinal cutoff of VLF signals in the ionosphere. *J. Geophys. Res.* **74**(9), 2393–2397 (1969)
- D. Ho, D.L. Carpenter, Outlying plasmasphere structure detected by whistlers. *Planet. Space Sci.* **24**(10), 987–994 (1976)
- J.L. Horwitz, R.H. Comfort, C.R. Chappell, A statistical characterization of plasmasphere density structure and boundary locations. *J. Geophys. Res.* **95**(A6), 7937–7947 (1990)
- X. Huang, B.W. Reinisch, Automatic calculation of electron density profiles from digital ionograms. 2. True height inversion of topside ionograms with the profile-fitting method. *Radio Sci.* **17**(4), 837–844 (1982)
- X. Huang, B.W. Reinisch, P. Song, J.L. Green, D.L. Gallagher, Developing an empirical density model of the plasmasphere using IMAGE/RPI observations. *Adv. Space Res.* **33**(6), 829–832 (2004)
- U.S. Inan, T.F. Bell, R.A. Helliwell, Nonlinear pitch angle scattering of energetic electrons by coherent VLF waves in the magnetosphere. *J. Geophys. Res.* **83**(A7), 3235–3253 (1978)
- D. Jones, Terrestrial myriametric radiation from the Earth's plasmopause. *Planet. Space Sci.* **30**(4), 399–410 (1982)
- Y. Kasaba, H. Matsumoto, K. Hashimoto, R.R. Anderson, J.-L. Bougeret, M.L. Kaiser, X.Y. Wu, I. Nagano, Remote sensing of the plasmopause during substorms: Geotail observation of nonthermal continuum enhancement. *J. Geophys. Res.* **103**(A9), 20389–20405 (1998)
- C.R. Kennel, H.E. Petschek, Limit on stably trapped particle fluxes. *J. Geophys. Res.* **71**(1), 1–28 (1966)
- G.V. Khazanov, M.W. Liemohn, T.S. Newman, M.-C. Fok, R.W. Spiro, Self-consistent magnetosphere-ionosphere coupling: Theoretical studies. *J. Geophys. Res.* **108**(A3), 1122 (2003)
- I. Kimura, Effects of ions on whistler-mode ray tracing. *Radio Sci.* **1**, 269–283 (1966)
- G.A. Kotova, The Earth's plasmasphere: State of studies (a review). *Geomagn. Aeron.* **47**(4), 409–422 (2007)
- G.A. Kotova, V.V. Bezrukhikh, M.I. Verigin, J. Smilauer, New aspects in plasmaspheric ion temperature variations from INTERBALL 2 and MAGION 5 measurements. *J. Atmos. Sol.-Terr. Phys.* **70**(2–4), 399–406 (2008)

- H. Laakso, A. Pedersen, Ambient electron density derived from differential potential measurements, in *Measurements Techniques in Space Plasmas: Particles*, ed. by R.F. Pfaff, J.E. Borovsky, D.T. Young. Geophysical Monograph Series, vol. 102 (American Geophysical Union, Washington, 1998), pp. 49–54
- H. Laakso, R. Pfaff, P. Janhunen, Polar observations of electron density distribution in the Earth's magnetosphere. 1. Statistical results. *Ann. Geophys.* **20**(11), 1711–1724 (2002)
- J.W. LaBelle, R.A. Treumann (eds.), *Geospace Electromagnetic Waves and Radiation*. Lecture Notes in Physics, vol. 687 (Springer, Berlin, 2006)
- B.A. Larsen, D.M. Klumpar, C. Gurgiolo, Correlation between plasmopause position and solar wind parameters. *J. Atmos. Sol.-Terr. Phys.* **69**(3), 334–340 (2007)
- M.J. LeDocq, D.A. Gurnett, R.R. Anderson, Electron number density fluctuations near the plasmopause observed by the CRRES spacecraft. *J. Geophys. Res.* **99**(A12), 23661–23671 (1994)
- J.F. Lemaire, The mechanisms of formation of the plasmopause. *Ann. Geophys.* **31**, 175–190 (1975)
- J.F. Lemaire, K.I. Gringauz, *The Earth's Plasmasphere* (Cambridge University Press, New York, 1998)
- M.W. Liemohn, P.C. Brandt, Small-scale structure in the storm time ring current, in *Inner Magnetosphere Interactions: New Perspectives from Imaging*, ed. by J.L. Burch, M. Schulz, H. Spence. Geophysical Monograph Series, vol. 159 (American Geophysical Union, Washington, 2005), pp. 167–177
- A. Masson, O. Santolík, D.L. Carpenter, F. Darrouzet, P.M.E. Décréau, J.L. Green, S. Grimald, F. El-Lemdani Mazouz, M.B. Moldwin, F. Němec, Advances in plasmaspheric wave research with CLUSTER and IMAGE observations. *Space Sci. Rev.* (2008, this issue)
- H. Matsui, J.C. Foster, D.L. Carpenter, I. Dandouras, F. Darrouzet, J. De Keyser, D.L. Gallagher, J. Goldstein, P.A. Puhl-Quinn, C. Vallat, Electric fields and magnetic fields in the plasmasphere: A perspective from CLUSTER and IMAGE. *Space Sci. Rev.* (2008, this issue)
- H. Matsumoto, I. Kimura, Linear and nonlinear instabilities and VLF emissions in the magnetosphere. *Planet. Space Sci.* **19**(6), 567–608 (1971)
- C.E. McIlwain, Coordinates for mapping the distribution of magnetically trapped particles. *J. Geophys. Res.* **66**(11), 3681–3691 (1961)
- D.G. Mitchell, S.E. Jaskulek, C.E. Schlemm, E.P. Keath, R.E. Thompson, B.E. Tossman, J.D. Boldt, J.R. Hayes, G.B. Andrews, N. Paschalidis, D.C. Hamilton, R.A. Lundgren, E.O. Tums, P. Wilson, H.D. Voss, D. Prentice, K.C. Hsieh, C.C. Curtis, F.R. Powell, High energy neutral atom (HENA) imager for the IMAGE mission. *Space Sci. Rev.* **91**(1–2), 67–112 (2000)
- M.B. Moldwin, L. Downward, H.K. Rassoul, R. Amin, R.R. Anderson, A new model of the location of the plasmopause: CRRES results. *J. Geophys. Res.* **107**(A11), 1339 (2002)
- M.B. Moldwin, B.R. Sandel, M.F. Thomsen, R.C. Elphic, Quantifying global plasmaspheric images with in situ observations. *Space Sci. Rev.* **109**(1), 47–61 (2003)
- M.B. Moldwin, M.F. Thomsen, S.J. Bame, D.J. McComas, K.R. Moore, An examination of the structure and dynamics of the outer plasmasphere using multiple geosynchronous satellites. *J. Geophys. Res.* **99**(A6), 11475–11481 (1994)
- T.E. Moore, D.J. Chornay, M.R. Collier, F.A. Herrero, J. Johnson, M.A. Johnson, J.W. Keller, J.F. Laudadio, J.F. Lobell, K.W. Ogilvie, P. Rozmarynowski, S.A. Fuselier, A.G. Ghielmetti, E. Hertzberg, D.C. Hamilton, R. Lundgren, P. Wilson, P. Walpole, T.M. Stephen, B.L. Peko, B. Van Zyl, P. Wurz, J.M. Quinn, G.R. Wilson, The Low Energy Neutral Atom imager for IMAGE. *Space Sci. Rev.* **91**(1–2), 155–195 (2000)
- S.R. Mosier, M.L. Kaiser, L.W. Brown, Observations of noise bands associated with the upper hybrid resonance by the IMP 6 radio astronomy experiment. *J. Geophys. Res.* **78**(10), 1673–1679 (1973)
- O. Moullard, A. Masson, H. Laakso, M. Parrot, P.M.E. Décréau, O. Santolík, M. André, Density modulated whistler mode emissions observed near the plasmopause. *Geophys. Res. Lett.* **29**(20), 1975 (2002)
- A. Nishida, Formation of plasmopause, or magnetospheric plasma knee, by the combined action of magnetospheric convection and plasma escape from the tail. *J. Geophys. Res.* **71**(23), 5669–5679 (1966)
- P.A. Nsumei, B.W. Reinisch, P. Song, J. Tu, X. Huang, Polar cap electron density distribution from IMAGE/RPI measurements: The relative importance of solar illumination and geomagnetic activity. *J. Geophys. Res.* **113**, A01217 (2008)
- D. Nunn, A self-consistent theory of triggered VLF emissions. *Plan. Space Sci.* **22**(3), 349–378 (1974)
- Y. Omura, H. Matsumoto, Computer simulations of basic processes of coherent whistler-mode wave-particle interactions in the magnetosphere. *J. Geophys. Res.* **87**(A6), 4435–4444 (1982)
- C.G. Park, Whistler observations of the interchange of ionization between the ionosphere and the protonosphere. *J. Geophys. Res.* **75**(22), 4249–4260 (1970)
- E.W. Paschal, R.A. Helliwell, Phase measurements of whistler mode signals from the Siple VLF transmitter. *J. Geophys. Res.* **89**(A3), 1667–1674 (1984)
- G. Paschmann, P.W. Daly (eds.), *Analysis Methods for Multi-Spacecraft Data*. ISSI SR-001 (ESA Publications Division, Noordwijk, 1998)

- G. Paschmann, P.W. Daly (eds.), *Multi-Spacecraft Analysis Methods Revisited*. ISSI SR-008 (ESA Communications, Noordwijk, 2008)
- G. Paschmann, J.M. Quinn, R.B. Torbert, H. Vaith, C.E. McIlwain, G. Haerendel, O.H. Bauer, T. Bauer, W. Baumjohann, W. Fillius, M. Förster, S. Frey, E. Georgescu, S.S. Kerr, C.A. Kletzing, H. Matsui, P. Puhl-Quinn, E.C. Whipple, The Electron Drift Instrument on Cluster: Overview of first results. *Ann. Geophys.* **19**(10–12), 1273–1288 (2001)
- G. Paschmann, S.J. Schwartz, C.P. Escoubet, S. Haaland (eds.), *Outer Magnetospheric Boundaries: Cluster Results*. Space Science Series of ISSI, vol. 20 (Springer, Dordrecht, 2005)
- A. Pedersen, Solar wind and magnetosphere plasma diagnostics by spacecraft electrostatic potential measurements. *Ann. Geophys.* **13**(2), 118–129 (1995)
- A. Pedersen, P. Décréau, C.P. Escoubet, G. Gustafsson, H. Laakso, P.-A. Lindqvist, B. Lybekk, A. Masson, F. Mozer, A. Vaivads, Four-point high resolution information on electron densities by the electric field experiments (EFW) on Cluster. *Ann. Geophys.* **19**(10–12), 1483–1489 (2001)
- A. Pedersen, B. Lybekk, M. André, A. Eriksson, A. Masson, F.S. Mozer, P.-A. Lindqvist, P.M.E. Décréau, I. Dandouras, J.-A. Sauvaud, A. Fazakerley, M. Taylor, G. Paschmann, K.R. Svenes, K. Torkar, E. Whipple, Electron density estimations derived from spacecraft potential measurements on Cluster in tenuous plasma regions. *J. Geophys. Res.* **113**, A07S33 (2008)
- V. Pierrard, J. Goldstein, N. André, V.K. Jordanova, G.A. Kotova, J.F. Lemaire, M.W. Liemohn, H. Matsui, Recent progress in physics-based models of the plasmasphere. *Space Sci. Rev.* (2008, this issue)
- C.J. Pollock, K. Asamura, J. Baldonado, M.M. Balkey, P. Barker, J.L. Burch, E.J. Korpela, J. Cravens, G. Dirks, M.-C. Fok, H.O. Funsten, M. Grande, M. Gruntman, J. Hanley, J.M. Jahn, M. Jenkins, M. Lampton, M. Marckwordt, D.J. McComas, T. Mukai, G. Penegor, S. Pope, S. Ritzau, M.L. Schattenburg, E. Scime, R. Skoug, W. Spurgeon, T. Stecklein, S. Storms, C. Urdiales, P. Valek, J.T.M. Van Beek, S.E. Weidner, M. Wüest, M.K. Young, C. Zinsmeyer, Medium Energy Neutral Atom (MENA) imager for the IMAGE mission. *Space Sci. Rev.* **91**(1–2), 113–154 (2000)
- J.L. Rauch, X. Suraud, P.M.E. Décréau, J.G. Trotignon, R. Ledée, G. Lemerrier, F. El-Lemdani Mazouz, S. Grimald, G. Bozan, X. Vallières, P. Canu, F. Darrouzet, Automatic determination of the plasma frequency using image processing on WHISPER data. *Proceedings of the Cluster and Double Star Symposium, 5th Anniversary of Cluster in Space*. **ESA SP-598** (2006)
- B.W. Reinisch, G.S. Sales, D.M. Haines, S.F. Fung, W.W.L. Taylor, Radio wave active Doppler imaging of space plasma structures: Arrival angle, wave polarization, and Faraday rotation measurements with the radio plasma imager. *Radio Sci.* **34**(6), 1513–1524 (1999)
- B.W. Reinisch, D.M. Haines, K. Bibl, G. Cheney, I.A. Galkin, X. Huang, S.H. Myers, G.S. Sales, R.F. Benson, S.F. Fung, J.L. Green, S. Boardsen, W.W.L. Taylor, J.L. Bougeret, R. Manning, N. Meyer-Vernet, M. Moncuquet, D.L. Carpenter, D.L. Gallagher, P. Reiff, The Radio Plasma Imager investigation on the IMAGE spacecraft. *Space Sci. Rev.* **91**(1–2), 319–359 (2000)
- B.W. Reinisch, X. Huang, P. Song, G.S. Sales, S.F. Fung, J.L. Green, D.L. Gallagher, V.M. Vasyliunas, Plasma density distribution along the magnetospheric field: RPI observations from IMAGE. *Geophys. Res. Lett.* **28**(24), 4521–4524 (2001)
- B.W. Reinisch, X. Huang, P. Song, J.L. Green, S.F. Fung, V.M. Vasyliunas, D.L. Gallagher, B.R. Sandel, Plasmaspheric mass loss and refilling as a result of a magnetic storm. *J. Geophys. Res.* **109**, A01202 (2004)
- B.W. Reinisch, M.B. Moldwin, R.E. Denton, D.L. Gallagher, H. Matsui, V. Pierrard, J. Tu, Augmented empirical models of plasmaspheric density and electric field using IMAGE and CLUSTER data. *Space Sci. Rev.* (2008, this issue)
- H. Rème, C. Aoustin, J.M. Bosqued, I. Dandouras, B. Lavraud, J.A. Sauvaud, A. Barthe, J. Bouyssou, Th. Camus, O. Coeur-Joly, A. Cros, J. Cuvilo, F. Ducay, Y. Garbarowitz, J.L. Médale, E. Penou, H. Perrier, D. Romefort, J. Rouzaud, C. Vallat, D. Alcaydé, C. Jacquy, C. Mazelle, C. d'Uston, E. Möbius, L.M. Kistler, K. Crocker, M. Granoff, C. Mouikis, M. Popecki, M. Vosbury, B. Klecker, D. Hovestadt, H. Kucharek, E. Kuenneth, G. Paschmann, M. Scholer, N. Scopke, E. Seidenschwang, C.W. Carlson, D.W. Curtis, C. Ingraham, R.P. Lin, J.P. McFadden, G.K. Parks, T. Phan, V. Formisano, E. Amata, M.B. Bavassano-Cattaneo, P. Baldetti, R. Bruno, G. Chionchio, A. Di Lellis, M.F. Marcucci, G. Pallochia, A. Korth, P.W. Daly, B. Graeve, H. Rosenbauer, V. Vasyliunas, M. McCarthy, M. Wilber, L. Eliason, R. Lundin, S. Olsen, E.G. Shelley, S. Fuselier, A.G. Ghielmetti, W. Lennartsson, C.P. Escoubet, H. Balsiger, R. Friedel, J.-B. Cao, R.A. Kovrazhkin, I. Papamastorakis, R. Pellat, J. Scudder, B. Sonnerup, First multi-spacecraft ion measurements in and near the Earth's magnetosphere with the identical Cluster ion spectrometry (CIS) experiment. *Ann. Geophys.* **19**(10–12), 1303–1354 (2001)
- A.D. Richmond, Self-induced motions of thermal plasma in the magnetosphere and the stability of the plasmopause. *Radio Sci.* **8**(11), 1019–1027 (1973)
- P. Robert, A. Roux, C.C. Harvey, M.W. Dunlop, P.W. Daly, K.-H. Glassmeier, Tetrahedron geometric factors, in *Analysis Methods for Multi-Spacecraft Data*, ed. by G. Paschmann, P.W. Daly. ISSI SR-001 (ESA Publications Division, 1998), pp. 323–348

- E.C. Roelof, A.J. Skinner, Extraction of ion distributions from magnetospheric ENA and EUV images. *Space Sci. Rev.* **91**(1–2), 437–459 (2000)
- B.R. Sandel, M.H. Denton, Global view of refilling of the plasmasphere. *Geophys. Res. Lett.* **34**, L17102 (2007)
- B.R. Sandel, A.L. Broadfoot, C.C. Curtis, R.A. King, T.C. Stone, R.H. Hill, J. Chen, O.H.W. Siegmund, R. Raffanti, D.D. Allred, R.S. Turley, D.L. Gallagher, The Extreme UltraViolet imager investigation for the IMAGE mission. *Space Sci. Rev.* **91**(1–2), 197–242 (2000)
- B.R. Sandel, J. Goldstein, D.L. Gallagher, M. Spasojević, Extreme ultraviolet imager observations of the structure and dynamics of the plasmasphere. *Space Sci. Rev.* **109**(1), 25–46 (2003)
- S.S. Sazhin, M. Hayakawa, K. Bullough, Whistler diagnostics of magnetospheric parameters: A review. *Ann. Geophys.* **10**(5), 293–308 (1992)
- G.P. Serbu, E.J.R. Maier, Low-energy electrons measured on IMP 2. *J. Geophys. Res.* **71**(15), 3755–3766 (1966)
- G.P. Serbu, E.J.R. Maier, Thermal plasma measurements within the magnetosphere, in *Space Research VII*, vol. 1, ed. by R.L. Smith-Rose, S.A. Bowhill, J.W. King (North Holland, Amsterdam, 1967), p. 527
- G.P. Serbu, E.J.R. Maier, Observations from OGO 5 of the thermal ion density and temperature within the magnetosphere. *J. Geophys. Res.* **75**(31), 6102–6113 (1970)
- R.R. Shaw, D.A. Gurnett, A test of two theories for the low-frequency cutoffs of nonthermal continuum radiation. *J. Geophys. Res.* **85**(A9), 4571–4576 (1980)
- D.R. Shklyar, F. Jiříček, Simulation of nonducted whistler spectrograms observed aboard the MAGION 4 and 5 satellites. *J. Atmos. Sol.-Terr. Phys.* **62**(5), 347–370 (2000)
- D.G. Sibeck, L. Prech, J. Safrankova, Z. Nemecek, Two-point measurements of the magnetopause: Interball observations. *J. Geophys. Res.* **105**(A1), 237–244 (2000)
- J. Smilauer, V. Truhlik, J. Boskova, P. Triska, J. Schultchishin, Observations of thermal  $O^{++}$  ions in the outer ionosphere. *Adv. Space Res.* **17**(10), 135–140 (1996)
- R.L. Smith, J.J. Angerami, Magnetospheric properties deduced from OGO 1 observations of ducted and nonducted whistlers. *J. Geophys. Res.* **73**(1), 1–20 (1968)
- B.U.Ö. Sonnerup, M. Scheible, Minimum and maximum variance analysis, in *Analysis Methods for Multi-Spacecraft Data*, ed. by G. Paschmann, P.W. Daly. ISSI SR-001 (ESA Publications Division, 1998), pp. 185–220.
- V.S. Sonwalkar, Magnetospheric LF-, VLF-, and ELF-waves, in *Handbook of Atmospheric Electrodynamics*, vol. II, ed. by H. Volland (CRC, Boca Raton, 1995), pp. 407–462
- V.S. Sonwalkar, The influence of plasma density irregularities on whistler-mode wave propagation, in *Geospace Electromagnetic Waves and Radiation*, ed. by J.W. LaBelle, R.A. Treumann. Lecture Notes in Physics, vol. 687 (Springer, Berlin, 2006), pp. 141–183
- M. Spasojević, J. Goldstein, D.L. Carpenter, U.S. Inan, B.R. Sandel, M.B. Moldwin, B.W. Reinisch, Global response of the plasmasphere to a geomagnetic disturbance. *J. Geophys. Res.* **108**(A9), 1340 (2003)
- S.M. Stankov, N. Jakowski, S. Heise, Reconstruction of ion and electron density profiles from space-based measurements of the upper electron content. *Planet. Space Sci.* **53**(9), 945–957 (2005)
- L.R.O. Storey, An investigation of whistling atmospherics. *Phil. Trans. R. Soc. (Lond.)* **246A**, 113–141 (1953)
- L.R.O. Storey, F. Lefeuvre, The analysis of 6-component measurements of a random electromagnetic wave field in a magnetoplasma. I. The direct problem. *Geophys. J. R. Astron. Soc.* **56**(2), 255–269 (1979)
- L.R.O. Storey, F. Lefeuvre, The analysis of 6-component measurements of a random electromagnetic wave field in a magnetoplasma. II. The integration kernels. *Geophys. J. R. Astron. Soc.* **62**(1), 173–194 (1980)
- H.A. Taylor Jr., H.C. Brinton, C.R. Smith, Positive ion composition in the magnetoionosphere obtained from the OGO-A satellite. *J. Geophys. Res.* **70**(23), 5769–5781 (1965)
- H.A. Taylor Jr., H.C. Brinton, M.W. Pharo III, Contraction of the plasmasphere during geomagnetically disturbed periods. *J. Geophys. Res.* **73**(3), 961–968 (1968)
- H.A. Taylor Jr., H.C. Brinton, D.L. Carpenter, F.M. Bonner, R.L. Heyborne, Ion depletion in the high-latitude exosphere: Simultaneous OGO 2 observations of the light ion trough and the VLF cutoff. *J. Geophys. Res.* **74**(14), 3517–3528 (1969)
- H.A. Taylor Jr., J.M. Grebowsky, W.J. Walsh, Structured variations of the plasmapause: Evidence of a corotating plasma tail. *J. Geophys. Res.* **76**(28), 6806–6814 (1971)
- M.F. Thomsen, D.J. McComas, J.E. Borovsky, R.C. Elphic, The magnetospheric trough, in *Geospace Mass and Energy Flow: Results from the International Solar–Terrestrial Physics program*, ed. by J.L. Horwitz, D.L. Gallagher, W.K. Peterson. Geophysical Monograph Series (American Geophysical Union, Washington, 1998), pp. 355–369.
- R.M. Thorne, E.J. Smith, R.K. Burton, R.E. Holzer, Plasmaspheric hiss. *J. Geophys. Res.* **78**(10), 1581–1596 (1973)

- J.G. Trotignon, P.M.E. Décréau, J.L. Rauch, O. Randriamboarison, V. Krasnosels'kikh, P. Canu, H. Alleyne, K. Yearby, E. Le Guirriec, H.C. Séran, F.X. Sené, P. Martin, M. Lévêque, P. Fergeau, How to determine the thermal electron density and the magnetic field strength from the CLUSTER/WHISPER observations around the Earth. *Ann. Geophys.* **19**(10–12), 1711–1720 (2001)
- J.G. Trotignon, P.M.E. Décréau, J.L. Rauch, E. Le Guirriec, P. Canu, F. Darrouzet, The Whisper relaxation sounder onboard Cluster: A powerful tool for space plasma diagnosis around the Earth. *Cosmic Res.* **41**(4), 369–372 (2003)
- N.A. Tsyganenko, D.P. Stern, Modeling the global magnetic field of the large-scale Birkeland current systems. *J. Geophys. Res.* **101**(A12), 27187–27198 (1996)
- J. Tu, P. Song, B. Reinisch, X. Huang, J.L. Green, H.U. Frey, P.H. Reiff, Electron density images of the middle- and high-latitude magnetosphere in response to the solar wind. *J. Geophys. Res.* **110**, A12210 (2005)
- C. Vallat, I. Dandouras, M. Dunlop, A. Balogh, E. Lucek, G.K. Parks, M. Wilber, E.C. Roelof, G. Chanteur, H. Rème, First current density measurements in the ring current region using simultaneous multi-spacecraft CLUSTER-FGM data. *Ann. Geophys.* **23**(5), 1849–1865 (2005)
- C. Wang, T.S. Newman, D.L. Gallagher, Plasmopause equatorial shape determination via the Minimum L Algorithm: Description and evaluation. *J. Geophys. Res.* **112**, A12201 (2007)
- S. Watanabe, B.A. Whalen, A.W. Yau, Thermal ion observations of depletion and refilling in the plasmaspheric trough. *J. Geophys. Res.* **97**(A2), 1081–1096 (1992)
- D.J. Williams, E.C. Roelof, D.G. Mitchell, Global magnetospheric imaging. *Rev. Geophys.* **30**(3), 183–208 (1992)